Ultrafast OPCPA system for amplification of ultrashort pulses and application of high intensity pulses to tabletop Lensless Imaging in the EUV region

Diplomarbeit

seit 1558

FRIEDRICH-SCHILLER-UNIVERSITÄT JENA
PHYSIKALISCH-ASTRONOMISCHE FAKULTÄT

eingereicht von Steffen Hädrich
geboren am 2. August 1982 in Jena

Betreuer:	Dr. rer. nat. J. Limpert
1. Gutachter:	Prof. Dr. rer. nat. habil. A. Tünnermann
2. Gutachter:	Prof. Dr. rer. nat. habil. H. Bartelt

Bearbeitungszeitraum: November 2006 - Oktober 2007
Tag der Verleihung des Diploms:.....

Acknowledgements

I gratefully acknowledge the help of many people who made the working on this thesis the most exciting part of my study. First of all I would like to thank Prof. Andreas Tünnermann for giving me the chance to work on a cutting-edge research topic, for supervising the work, and for supporting the visit at JILA at the University of Colorado (Boulder, Colorado). In addtion, I thank Prof. Margaret Murnane and Prof. Henry Kapteyn for welcoming me into their research group and making it possible to join their lensless imaging project.

In particular, I thank Richard Sandberg, Ariel Paul, and Luis Miaja-Avila for a great working atmosphere, for being friends, and for introducing me to the American culture. Thanks to Brandon Smith, Stefan Matthias, and Nathan Kirchhofer for having so much fun inside and outside the lab. Thank you to all the members of the group: Guido Saathoff, Daisy Raymondson, Mark Siemens, Amy Lytle, Tenio Popmintchev, Arvinder Sandhu, Xiaoshi Zhang, Qing Li, Robynne Hooper, Xibin Zhou, Isabell Thomann, Etienne Gagnon, Nicholas Wagner, Wen Li, Oren Cohen, Ming-Chang Chen and Rachael Tearle. I really enjoyed my time with you guys.

Equally, I would like to say thanks to all the members of the fiber and waveguide lasers group at the Institute of Applied Phyics at the Friedrich Schiller Universität Jena: Fabian Röser, Oliver Schmidt, Damian Schimpf, Tino Eidam, Bülend Ortaç, Dirk Nodop, Katja Rademaker, Thomas Schreiber, Doreen Müller, Marko Plötner, Andreas Martin, Sebastian Linke, Sandro Klingebiel.

Special thanks go to Jens Limpert and Jan Rothhardt for their assistance in setting up experiments in the lab and for their patience in answering my questions during the work on this project.

Finally, I acknowledge support of the German Academic Exchange Service (DAAD) during my stay at Boulder.

Thanks to my family for supporting me throughout the whole study and to you, Maren, for all your love and encouragement that helped me so much.

Contents

Chapter 1

Introduction

The Natural sciences strive to teach people about life and the inner workings of nature that govern life's existence. To improve the understanding of biology, chemistry and physics powerful tools to explore life on the smallest possible length and time scales inevitably are required. Many approaches exist that lead to the discovery of new phenomena, but perhaps recently, one of the most promising and exciting is the field of ultrashort optics that has arisen not long after the invention of the laser in 1960 [1], [2].
Ever since this invention, tremendous effort has been made to push the output of this unique coherent light source to shorter pulse durations, higher output energies, larger tuning ranges and higher peak powers. State-of-the-art laser systems can provide peak powers up to the Petawatt level, opening the way for the completely new field of high field physics [3], [4]. Acceleration of particles, e.g. protons [5], [6], or the generation of high temperature states of matter [7] have been key aspects of research in this field.
However, pulses on the femtosecond (10^{-15} s) time scale, allow researchers to study or even manipulate chemical reactions [8], while the large tuning ranges greatly benefits biology by enabling techniques such as fluorescence lifetime imaging (FLIM, [9]).
To explore new wavelength ranges, nonlinear frequency conversion can be applied. Shortly after the demonstration of the ruby laser [2], second harmonic generation (frequency doubling) was observed by Franken *et. al* [10]. Today, sum and difference frequency conversion are routinely used nonlinear processes to convert high intensity coherent laser radiation to new wavelengths.
A unique conversion technique is the extreme nonlinear phenomenon of high harmonic generation (HHG) observed for the first time in 1987 [11] and 1988 [12]. For intensities high enough to ionize an atom, an oscillating laser field can induce recombination processes that lead to the radiation of photons with a frequency that is an odd multiple of the fundamental. In this way, harmonic orders well above 100 can be generated [13], [14].

Maybe most exciting is the capability of this technique to provide enough bandwidth for the generation of attosecond pulses (10^{-18} s) that allow previously inaccessible phenomena to be studied [15]. Commonly, high harmonics are generated by focusing ultrashort high-peak-power pulses onto a gas jet, hence, generating intensities of the order of 10^{13} - 10^{15} W/cm^2. However, a modified approach takes advantage of a hollow-core gas-filled waveguide geometry and has demonstrated improved conversion efficiencies [16]. This technique allows for the generation of spatially and temporally coherent radiation in the sub-100 nm wavelength range. For microscopy purposes, this radiation holds great interest, since the smallest features that can be observed are (theoretically) of the order of the wavelength used to image. At synchrotron facilities imaging techniques making use of spatially-coherent short-wavelength light have been demonstrated [17] and can be adapted to HHG [18].

Today's laser systems used to generate the high harmonics are based on Ti:Sapphire oscillators and amplifiers that are limited by thermo-optical effects such as thermal lensing. These effects restrict the repetition rates to several kilohertz even with techniques like cryogenic cooling [19].

In contrast, fiber laser systems are nearly immune to thermal problems, since the large ratio of surface to active volume leads to excellent heat dissipation [20]. Based on chirped pulse amplification (CPA), the output of fiber lasers and amplifiers can be pushed to more than 100 W average power in the femtosecond range [21], [22] while pulse energies of 1 mJ can be achieved [23]. Unfortunately, they can not provide pulse durations of a few-10 fs [24].

A sophisticated technique to combine ultrashort pulse generation and amplification with high average powers are optical parametric amplifiers (OPA). These devices do not suffer from thermal problems, since no energy is stored in the crystal. Additionally, they offer a large amplification bandwidth, when nonlinear crystals such as BBO or LBO are used. High gain factors (10^4 to 10^6) and short crystal lengths (only a few mm) makes OPA suitable to generate pulses as short as 4 fs [25]. Owing to this outstanding characteristics, ultrashort pulse sources based on parametric amplification provide an attractive pump source for high-harmonic generation.

Fiber lasers constitute an excellent pump source for a high repetition rate OPA, due to their average power scalability. However, to generate and amplify ultrashort pulses a broadband seed signal is required. Continuum radiation can be generated by using a small portion (<10%) of the fiber laser system for filamentation in bulk substrates [26], e.g. Sapphire. Another technique relies on supercontinuum generation in highly nonlinear photonic crystal fibers [27], which has been used to demonstrate a broadband tunable (700 nm - 1500 nm) source [28].

A different approach for providing continuum radiation is presented in this thesis. The optical parametric amplifier is directly seeded with Ti:Sapphire oscillator pulses. Advantageously, these pulses promise a good compressibility, since they do not suffer from nonlinear phase terms. Additionally, the system works without an external pump laser for the OPA, and therefore, provides inherent synchronization. Overall, a detailed study of optical parametric chirped pulse amplification systems (OPCPA) based on fiber amplifier technique is unveiled. The feasibility of generating high-energy ultrashort pulses is investigated and possible applications for imaging techniques are discussed and emphasized by experiments using high-harmonic radiation.

The goal of the work is the amplification of a cavity dumped Ti:Sapphire oscillator at repetition rates as high as 2 MHz and with pulse durations shorter than 30 fs. Splitting the oscillator output to use it both as pump and seed source for an (OPCPA) system ensures synchronization.
Nonlinear frequency conversion in photonic crystal fibers is used to convert the 800 nm - 850 nm output of the oscillator to the amplification bandwidth of Ytterbium by generating a pulse at 1030 nm. Subsequent amplification is realized in a classical fiber based CPA system. The pulses are stretched to more than 300 ps to reduce nonlinear effects during amplification and later compressed by two gold-coated reflection gratings. The frequency doubled output is used to amplify the Ti:Sapphire pulses in a Beta Barium Borate (BBO) crystal. Finally, they are compressed in a fused silica prism compressor. Shorter pulses are obtained by increasing the signal bandwidth by self phase modulation (SPM) in a photonic crystal fiber.
Lensless imaging with coherent high-harmonic radiation is realized so as to investigate the requirements of pump sources for high-harmonic generation, which is of great interest for possible applications of the OPCPA system. A cryogenically cooled Ti:Sapphire amplifier output is focused into an Argon filled hollow-core waveguide producing spatially-coherent radiation at 29 nm that is slightly focused onto a sample. The far field diffraction pattern is recorded with an x-ray CCD camera, and a genetic iterative phase-retrieval algorithm is used to reconstruct the sample structure from the diffraction pattern.

The work is structured as follows: In chapter 2 the basics of high-harmonic generation are described and the results of the lensless imaging experiment are presented. The theoretical elements necessary to understand the fiber laser pumped optical parametric amplification presented here are provided in chapters 3, 4 and 5. A detailed characterization of the OPCPA system, including all experimental requirements, setups and results, can be found in chapter 6. The thesis concludes with a summary and also gives an outlook to future experiments and possibilities.

Chapter 2

High harmonic generation and lensless imaging

Since the first observation of High Harmonics in 1987 [11],[12], tremendous effort has been applied in this field of research, both theoretically and experimentally. One of the most interesting qualities of the generation of high harmonics is their capability of providing enough bandwidth to generate single attosecond pulses. Such pulses provide a unique tool for studies of electron motion, evolution of molecules in highly excited states and the evolution of molecular hydrogen, a system well described in theory, but still not accessible to experiments validating this theory [29].
Chapter 5 describes how the material responds to high intensity laser fields. When electrons move in a non-parabolic potential, the polarization is a nonlinear quantity that leads to interesting effects. Thinking of even more intense laser fields with intensities high enough to ionize the atom, it is imaginable that there will be exciting new phenomena to explore.
This chapter gives a short introduction to high-harmonic generation (HHG), one of the most intense research fields in the current decade. After introducing a semi-classical model a lensless imaging technique is discussed as application.

2.1 High Harmonic Generation

By focusing ultrashort pulses onto a gas medium, intensities high enough to ionize the gas (10^{13} to 10^{15} W/cm^2) can be generated. The nonlinear interaction of the highly intense laser light with atoms can lead to the generation of odd harmonics. A schematic spectrum with certain characteristic features for this process is shown in figure (fig. 2.1).

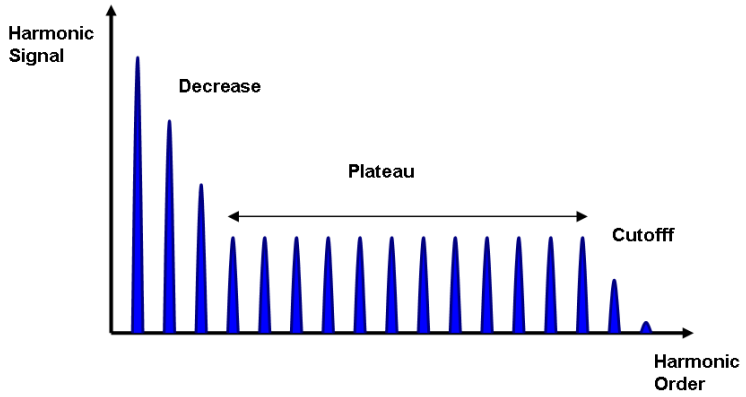

Figure 2.1: Schematic spectrum for High Harmonic Generation.

The spectrum consists of evenly spaced lines that are separated by twice the fundamental laser frequency, and therefore, provides odd harmonics with frequencies $\omega_q = q \cdot \omega_0 = (2n+1)\omega_0$. The efficiency decreases very quickly over the first harmonic orders. The higher-order harmonics form a broad plateau over which the efficiency is roughly the same and then immediately disappears for frequencies higher than ω_c. The cutoff frequency ω_c depends sensitively on the gas medium and the fundamental laser properties, such as frequency ω_0, pulse duration τ, intensity I and polarization state (eq. 2.7).

2.1.1 Semiclassical Picture of High Harmonic Generation

Full quantum mechanical models can only be solved numerically, but consideration of a semiclassical model proves quite instructive [30], [31]. This model describes most of the experimental effects and also gives an explanation for the cutoff frequency. The semiclassical approach is only valid in the so-called tunnel regime

$$\hbar\omega_0 \ll I_p \ll U_p, \tag{2.1}$$

where I_p is the ionization potential of the atom, U_p is the ponderomotive energy (eq. 2.5) corresponding to the average kinetic energy of a free electron oscillating in the laser field, and ω_0 is the frequency of the driving laser field.
To fully understand the semiclassical approach to high-harmonic generation, some basic considerations relating to atomic ionization should be taken into account.

Ionizing an atom in the Tunnel Regime

Necessarily, equation 2.1 implies that an atom can only be ionized after absorbing multiple photons. In this simple model, the photonic character of the light can be partly neglected.
The easiest way to describe this system is to consider the atom as an ionic core with a single electron. The former creates a Coulomb potential the electron is evolving and the intense laser field is described as a slowly oscillating electric field $E(t) = E_0(t)\cos(\omega_0 t)$. Once the atom is irradiated by the strong laser field, the total potential seen by the electron is the sum of the Coulomb potential and the electric interaction potential

$$U_{total} = \underbrace{U_C}_{\text{Coulomb potential}} + \underbrace{q \cdot \vec{E} \cdot \vec{r}}_{\text{electric interaction potential}} , \tag{2.2}$$

where q is the electric charge, $\vec{E}$ the applied electrical field and $\vec{r}$ the distance of the electrical charge to the electrical field.

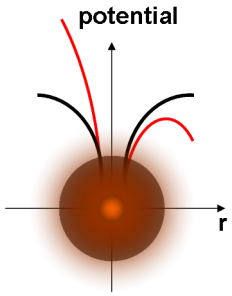

Figure 2.2: Schematic of the Potential seen by the electron without (black) and with (red) an intense laser field.

The behavior of the potential when an intense laser field is applied to the atoms Coulomb potential is shown in figure 2.2. There is a potential barrier in direction of the driving field (red potential in fig. 2.2) through which the electron can tunnel with a probability that is derived in [32]. This probability depends on the initial energy level and the width of the barrier, which is defined by the field strength.

Free electrons in electrical fields

To ionize the atom, the electron has to be released in the strong electric field of the driving laser light, implying that its motion is strongly determined by the electric force. For

that reason, the core attraction can be neglected and the motion of a free electron has to be investigated. Note that the time of ionization t_i has a great influence on the motion. Speaking classically, the equation of motion for an electron with mass m is

$$m\frac{\partial^2 x}{\partial t^2} = qE\cos(\omega_0 t) \tag{2.3}$$

for a field linearly polarized in x direction.
The electron velocity in the slowly varying envelope approximation is derived by a simple integration of 2.3 and can be written as

$$v(t) = \frac{qE}{m\omega_0}\cdot(\sin(\omega_0 t) - sin(\omega_0 t_i)) + v_0, \tag{2.4}$$

where v_0 is the initial velocity. Assuming that the electron is released without kinetic energy ($v_0 = 0$), the average kinetic energy, termed ponderomotive energy, is

$$\overline{E_{kin}} = \frac{m}{2}\overline{v^2} = U_p = \frac{q^2E^2}{4m{\omega_0}^2}. \tag{2.5}$$

The energy that is provided by the laser field to the electron is on the order of U_p. A further integration of 2.4 provides the trajectory

$$x(t) = \frac{qE}{m\omega_0}\left[\frac{1}{\omega_0}(\cos(\omega_0 t_i) - \cos(\omega_0 t)) - \sin(\omega_0 t_i)(t - t_i)\right] \tag{2.6}$$

of the electron after being ionized. Equation 2.6 shows that the electron is ripped off the atom ($x = 0$) at the time t_i and can bounce back to its parent ion after a certain return time t_r that is determined by 2.6.
The kinetic energy an electron gains until it recombines can be calculated with the help of 2.4 and 2.6 as a function of the ionization phase $\varphi_i = \omega_0 t_i$.
Figure 2.3 shows the dependence of the kinetic energy with respect to the ionization phase. For an ionization phase of $\omega_0 t_i = 18^\circ$ the electron has a maximum kinetic energy of $E_{kin} = 3.17 \cdot U_p$. Hence, this simple approach provides the well-known cutoff law for high harmonic generation

$$\hbar\omega_c = I_p + 3.17 \cdot U_p, \tag{2.7}$$

where $\hbar\omega_c$, I_p and U_p are the maximum photon energy, the ionization potential, and the ponderomotive energy, respectively. Since $U_p \propto E^2 (\propto I)$ (see Eq. (2.5)) the order of emitted harmonics can be increased by applying high-intensity laser radiation to atoms with high ionization energies, such as noble gases.

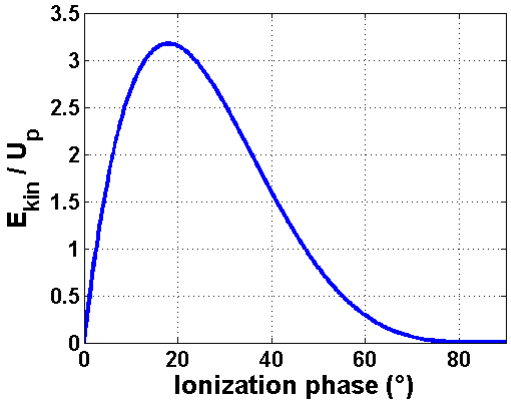

Figure 2.3: Kinetic Energy of the electron at its first return to the parent ion as a function of the ionization phase. The electron is released with no kinetic energy at the initial position (x=0).

Three Step Model

Finally, the insights of the preceding discussion can be summarized in a "simple man model" known as three step model:

1. An atom is ionized at a time t_i by an intense laser field. A parent ion and a free electron with no initial kinetic energy are created.

2. The free electron is accelerated by the electrical field of the laser light. When this changes its sign there is a certain probability that the electron can be found in the vicinity of its parent ion.

3. In the event of a collision with the parent ion the electron recombines and releases its energy, i.e. its kinetic energy and the binding energy of the atom, by emitting a photon of energy $\hbar\omega = E_{kin} + I_p$.

The emission of such a EUV photon strongly depends on the probability to ionize the atom. This probability is largest when the electric field has a maximum, and therefore, has a periodicity of half an optical cycle of the fundamental. In a more detailed investigation the electron, of course, must be considered as quantum wave packet with its own phase. Initially, there is a transition of the wave function (atomic ground state) to the continuum, then an evolution of the wave packet in the continuum and finally a transition back to the ground state associated with the emission of radiation (fig. 2.4).

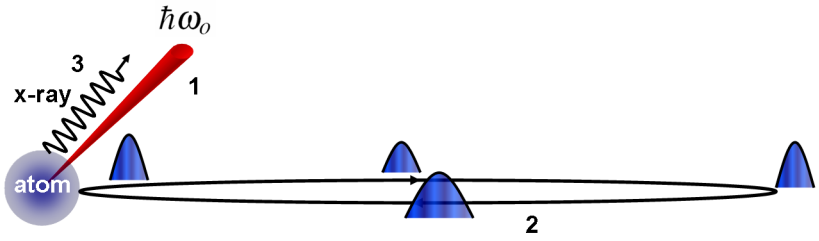

Figure 2.4: Three step model: The atom is irradiated by the intense laser field ($\hbar\omega_0$) and ionized (1). The free electron wave packet evolves in the electrical field (2) and can make a transition back to the initial state linked with the emission of x-ray radiation (3).

This point of view reveals a very important feature of this process. Due to the fact that the phase of the radiation is imposed by the evolution of the wave packet it is also locked to the phase of the fundamental driving laser field, resulting in a coherent process. Furthermore, the spatial coherence of the laser field is transferred to the high-harmonic beam, making it suitable for lensless-imaging techniques.
The emission of a macroscopic medium can be obtained by summing all amplitudes of the particular atoms. The total intensity is the square of the total amplitude and reveals that collective effects, such as phase matching and reabsorption, also play an important role in that radiation process.
A deeper insight to high harmonic generation necessarily requires a complete quantum mechanical analysis that can be found in several publications, e.g. [33].

2.2 Phase matching techniques for the Generation of High Harmonics

The investigation of nonlinear phenomena in chapter 5 reveals that for efficient conversion processes in bulk media, i.e. an ensemble of atoms and/or molecules, the fundamental and generated frequencies have to travel with the same velocity. Common techniques include phase matching via the birefringence of crystals or the temperature dependence of the index of refraction. Unfortunately, bulk materials are highly absorptive for extreme ultraviolet (EUV) radiation and gases, in which the harmonics are generated, are not birefringent. In the late 1990's a new approach to phase match high-harmonic generation in hollow waveguides was found [16]. The basic idea is to use a gas-filled hollow-core fiber that maintains a high intensity of the driving laser field and, furthermore, allows the

dispersion of the gas to be tailored by the means of the pressure. The phase mismatch $\Delta\vec{k}$ for the qth harmonic

$$\Delta\vec{k} = \vec{k}_q - q \cdot \vec{k}_0, \tag{2.8}$$

in a gas filled waveguide can be written as [34]

$$\Delta k \approx \frac{q\lambda_0\mu_{11}^2}{4\pi a^2} + P\left[\eta N_{atom} r_e(q\lambda_0 - \lambda_q) - \frac{2\pi(1-\eta)\Delta(\delta)}{\lambda_q}\right], \tag{2.9}$$

where $\Delta(\delta) = \delta(\lambda_0) - \delta(\lambda_q)$ is a function corresponding to the dispersive characteristics of the gas, μ_{11} is the first root of the Bessel function of zeroth kind J_0, a the waveguide diameter, P is the gas pressure, η the ionized fraction, N_{atom} is the number density of atoms at atmospheric pressure, and r_e is the classical electron radius, respectively. Equation 2.9 shows, that phase matching, i.e. $\Delta k = 0$, can be achieved for low levels of ionization by tuning the pressure [35]. Pressure tuning works well for ionization levels η <5%, since for higher levels of ionization the second term in equation 2.9 has the same sign as the first one. For efficient generation of the highest order harmonics (that correspond to high ionization levels) the limitations of pressure tuned phase matching have to be overcome. A very promising approach was introduced by Christov *et. al.* [36], [37]. They adapted an approach also known in "conventionial" nonlinear optics, namely quasi phase matching (QPM). In chapter 5 it is shown that for a phase difference, i.e. $\Delta k \neq 0$, energy can transfer back to the fundamental after propagating more than a coherence length. The QPM idea suggests to periodically alter the nonlinearity either by changing its strength, reversing its sign or eliminating it after each coherence length to enhance the output signal.
For HHG in hollow-core fibers a periodically modulation of the waveguides inner diameter (upper left corner in fig. 2.5) provides QPM and can be achieved by an unique glass-blowing setup (developed by A. Paul at JILA, Boulder). Assuming that the laser mode adiabatically follows the modulation results in a periodicity of the intensity distribution along the propagation direction. Naturally, the intensity is highest for the smallest spot size, i.e. for a shrunk part of the waveguide. Equation 2.7 says that the highest harmonic orders belong to the highest intensities, since $U_p \propto I$. Therefore the highest order harmonics are only generated in specific parts of the waveguide that are denoted by a "+" in figure 2.5. If the periodicity of the modulation is chosen to be a coherence length then a signal will only be generated over every other coherence length. So , the signal can add coherently and lead to enhanced conversion efficiencies for the highest order harmonics (fig. 2.5).

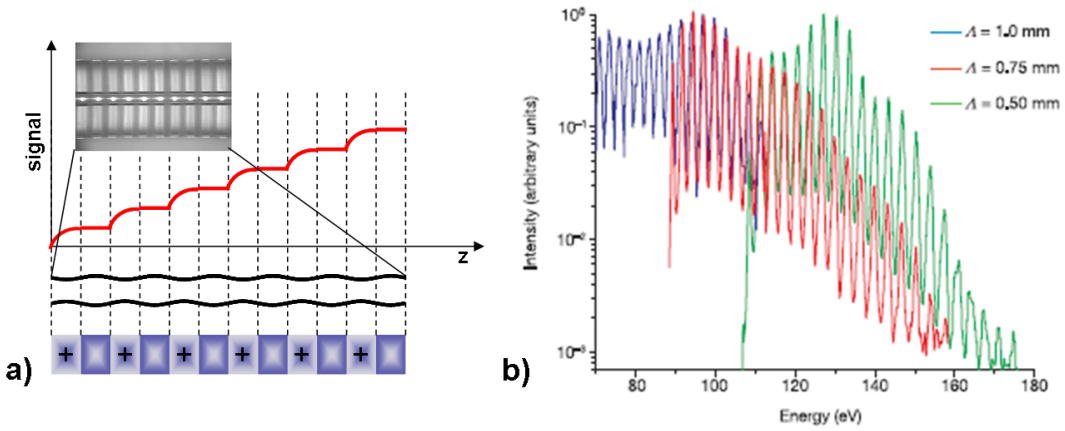

Figure 2.5: a) Schematic of the QPM process itself. The picture in the upper left corner shows a microscope picture of a waveguide with a modulation period of 0.25mm (from [38]). b) Experimental results for enhanced HHG with QPM (from [39]).

2.3 Lensless imaging with coherent EUV light

The preceding sections described some basics concerning HHG, especially in hollow-core waveguides. Since this process generates spatially coherent radiation, some interesting applications can be conceived.
Resolution of light microscopy is fundamentally limited by the wavelength of the illumination light, and therefore, the much shorter wavelength of the high-harmonic radiation appears very promising. Other imaging techniques, e.g. scanning electron microscopy (SEM) or scanning tunneling microscopy (STM), have shown resolution even on atomic scales, but are limited to thin samples or surfaces. EUV light can be used to image thick samples while maintaining a high resolution. Eminently important is the inherent image contrast due to various core-level absorption edges and widely varying elemental absorption cross sections. The "water window" (300 eV-500 eV) is especially interesting, since carbon is 10 times more absorbing than water in this region. Generally, imaging techniques in the soft-x-ray region rely on diffractive or reflective optics, e.g. Fresnel zone plates or multilayer mirrors, to image an object. However, lensless imaging is a relatively new coherent imaging technique that replaces the optical elements with a computerized algorithm, and was first demonstrated in 1999 [17].

2.3.1 Idea of lensless imaging and the phase problem

The idea of lensless imaging is very simple. A spatially coherent x-ray beam illuminates an object. Due to the coherence a diffraction pattern is generated in the far field of the object that is collected with a CCD camera and subsequently analyzed by the phase-retrieval algorithm to reconstruct the spatial structure of the specimen (fig. 2.6).

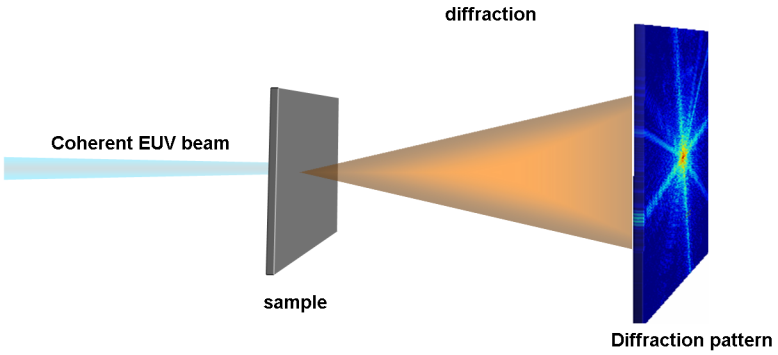

Figure 2.6: Lensless imaging. An object is illuminated by a coherent high harmonic beam and the far field diffraction pattern is collected with an x-ray CCD.

Since only the intensity ($\propto |E|^2$) is detected, a main issue of this experiment is to retrieve the phase without which it is impossible to find a reconstruction.

2.3.2 Phase retrieval algorithm and experimental requirements

J. Miao *et. al.* have found a way to solve the phase problem by oversampling the diffraction pattern, i.e. the diffraction peaks have to be sampled at a higher rate than the Nyquist frequency [40], [41]. Since a detailed discussion of this algorithm is far beyond the scope of this work only a sketch will be given. Figure 2.7 shows the basic idea of the phase-retrieval algorithm. Initially, a set of random phases is added to the square root of the collected diffraction pattern, resulting in a function with both amplitude and phase and then an inverse Fourier transform is applied.
The knowledge of the oversampling ratio[1] allows the application of constraints. Basically, a no density region surrounding the object exits in real space, corresponding to the oversampling ratio. After carefully setting the surrounding to zero a Fourier transform

[1]The oversampling ratio is the ratio of sampling to Nyquist frequency.

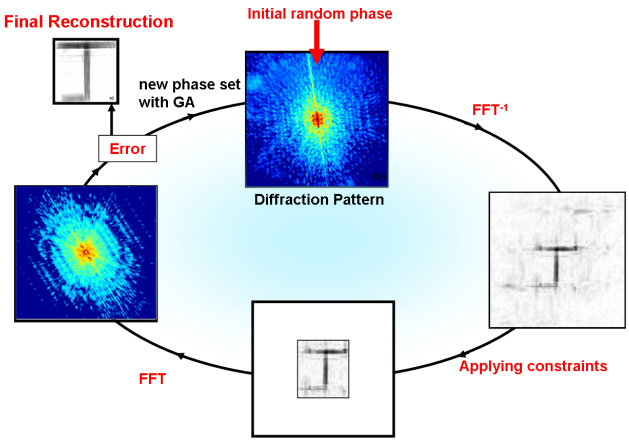

Figure 2.7: Scheme of the phase retrieval algorithm.

is performed to retrieve a diffraction pattern and a new set of phase functions. An error analysis selects the diffraction pattern that is closest to the collected one, and uses the corresponding phase function to run the algorithm again until the deviation is suitably small. Finally, the genetic algorithm yields a phase set that leads to the reconstruction of the sample.

There are several experimental parameters that have to be considered, e.g. the placement of the sample with respect to the detector, the parameters of the illuminating light, et cetera. To obtain a diffraction pattern, the sample has to be illuminated with a plane wave, which means that the sample aperture should be smaller than the radius of curvature of the wavefront. The distance z between sample and detector must also be chosen so as to fulfill

$$z \gg \frac{D^2}{\lambda}, \tag{2.10}$$

where D is the sample diameter and λ the wavelength of the illuminating light. Equation 2.10 is known as Fraunhofer criterion. Additionally, z has to be chosen in such a way that an appropriate oversampling ratio ($O > 5$) can be obtained, since this ratio can be expressed in terms of experimental parameters

$$O = \frac{z\lambda}{Dp}, \tag{2.11}$$

where p is the pixel size of the camera. In the reconstructed image the pixel size r (not to

be confused with a CCD pixel) is

$$r = \frac{OD}{N} = \frac{z\lambda}{pN}, \tag{2.12}$$

where N is the linear number of pixels. The value of r gives a limit of resolution, since one pixel is the ultimate feature size that can be discerned. Another limit is given by the nature of diffraction itself, since the smallest structures d diffract the incident light in an angle θ given by

$$d \sin\theta = \lambda. \tag{2.13}$$

Finally, the finite spectral bandwidth of the illuminating EUV source gives rise to another limitation. Miao *et. al.* [42] have found the requirements to be

$$\frac{\lambda}{\Delta\lambda} \geq \frac{OD}{d}. \tag{2.14}$$

To find a suitable geometry for lensless imaging equations 2.10 to 2.14 have to be balanced.

2.3.3 Experimental setup and results

Recently tabletop lensless imaging has been demonstrated with spatially-coherent light from HHG in hollow-core waveguides [18].

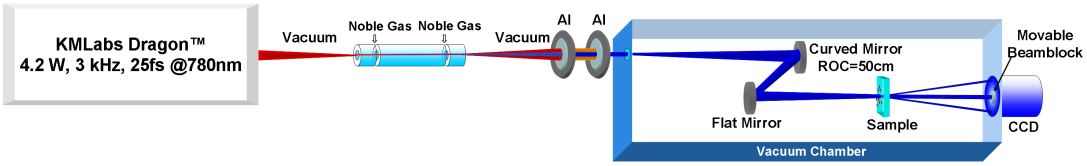

Figure 2.8: Experimental setup for tabletop lensless imaging.

The experimental setup is shown in figure 2.8. To generate the high harmonics a Ti:Sapphire amplifier system (KMLabs Dragon™) based on a multipass amplification in a cryogenically cooled crystal is used [43]. The amplifier runs at a repetition rate of 3 kHz and produces pulses centered at 780 nm with 25 fs pulse duration and an average power of 4.2 W, resulting in a pulse energy of 1.4 mJ. The entire setup is isolated against air currents and the waveguide and subsequent chamber are held under vacuum, since EUV light is highly absorbed by materials and air. For the purpose of HHG, the laser beams are focused into a 150 μm inner diameter capillary filled with Argon at 87 mbar ($\sim$65 torr)

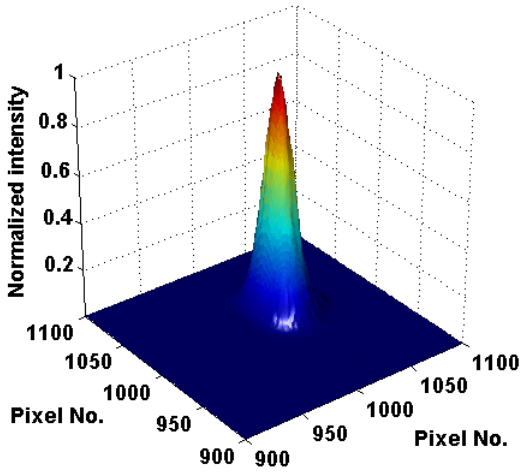

Figure 2.9: Measured EUV mode at an Argon pressure of 87 mbar (∼65 torr)

producing approximately five harmonics centered at the 27^{th} harmonic (29 nm, 45 eV), in a near Gaussian EUV mode (fig.2.9).
Two 200 nm thick Aluminum filters are used to block the fundamental photons while transmitting the EUV photons. To select a single harmonic a pair of narrowband Mo/Si multilayer mirrors is used. The first one has a radius of curvature of 50 cm to slightly focus the EUV beam onto the sample while the second one is flat. All mirrors and the sample are mounted with small piezo actuators, giving the ability to perform alignment in vacuum. The diffraction pattern is collected with an Andor DO436 x-ray CCD camera containing a chip of 2048×2048 pixels each with a size of 13.5 μm×13.5 μm.
Before running the experiment, amplified spontaneous emission (ASE) is used to align both the coupling to the waveguide and the beam path in the vacuum chamber. Next, the system is pumped down and the EUV flux and mode are optimized with the amplified ultra short Ti:Sapphire pulse by waveguide alignment and tuning the gas pressure. Finally, the piezo motors on the mirrors allow the EUV beam to be steered on the center of the camera. After venting the system, the sample is put in place and its aperture is aligned to transmit the beam emerging from the waveguide end (again ASE is used to align). To obtain the brightest diffraction pattern, minor tweaks to the sample translation stage are again necessary after evacuating the chamber. For high-quality reconstructions it is essential to use the full dynamic range of the camera. Unfortunately, the bright center of the diffraction pattern leads to a fast saturation of the camera, and therefore, the high spatial frequency information (that belong to the smallest structures) cannot be captured. To in-

crease the dynamic range, beam blocks of various size are used and mounted on a movable ring. They block the central part of the diffraction pattern and allow for longer integration times. So, a set of diffraction patterns is collected and ultimately stitched together and reconstructed by the group of John Miao (University of California, Los Angeles).

J-Slit aperture

A first simple specimen is used in order to learn about the limitations and capabilities of the system before the resolution is pushed. An aperture in form of a "J" about 80 μm tall is placed at a distance of z=33 cm, giving an oversampling ratio of O=9 (eq. 2.11) and an image pixel size of 0.35 μm (eq. 2.12).

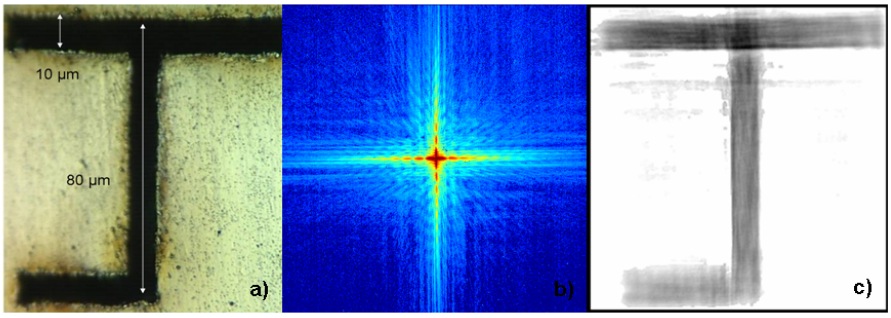

Figure 2.10: a)Microscope image of the J-Slit showing the dimensions. b) Stitched diffraction pattern. c) Final reconstruction of the J-Slit.

Results for this sample are shown in figure 2.10. Figure 2.10 b) was obtained by stitching 3 diffraction pattern together. The first one was taken without a beamblock, the second with a 200 μm block in 10 minutes and the last one with a 3 mm diameter beam block in 120 minutes. Finally, the reconstruction (fig.2.10 c)) clearly shows the "J" while maintaining the aspect ratio.

Quantifoil® Sample

The second sample is an electron microscope test grid manufactured by Quantifoil Micro Tools GmbH (Jena, [44]). The sample itself is coated with 20 nm-30 nm of gold to increase the opacity and a 15 μm aperture is put on top of it. Placing this sample 10 cm before the CCD camera gives an oversampling ratio of 14.5 and an image pixel size of 106 nm.

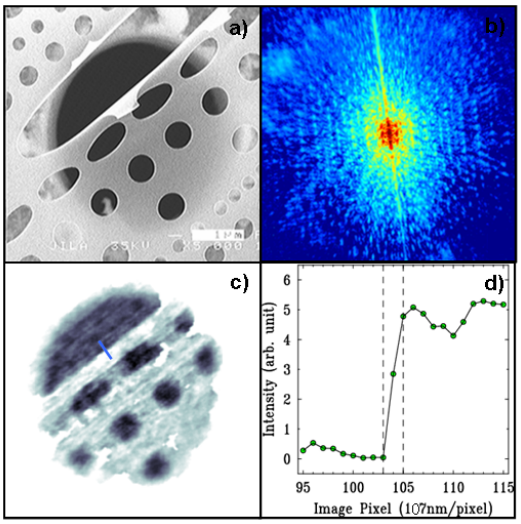

Figure 2.11: Experimental results for the Quantifoil®. a) SEM image of the test sample. b) Stitched diffraction pattern. c) Final reconstruction. d) Line scan taken at the blue line in c).

Figure 2.11 a) shows a scanning electron microscopy (SEM) image of the Quantifoil taken in the Keck Lab at JILA. The final diffraction pattern (fig.2.11 b)) is made up of 3 single patterns, and an analysis of the speckles near the edges leads to an estimated $\lambda/\Delta\lambda \approx 200\,\text{nm}$. This estimate agrees with measurements taken under the same experimental conditions, i.e. laser parameters, pressure and Argon gas. The reconstructed image (fig. 2.11 c)) with the corresponding line scan (fig. 2.11 d)) gives a resolution of 214 nm. The slight displacement of the aperture in the SEM and reconstructed image results merely from parallax, because the sample and aperture are separated by approximately $50\,\mu\text{m}$. Considering this fact, it is amazing that the aperture outline can be seen clearly in the reconstructed image, thus, the depth of field is large.

2.4 Summary

A tabletop lensless imaging system based on HHG in gas-filled hollow-core waveguides has been realized, and impressive and encouraging results have been obtained. The pulse parameters of the pump source for high-harmonic generation have to be adequate to achieve sufficient intensities, that enable this extreme nonlinear process. For this particular experiment the intensity is roughly 10^{14} W/cm^2 and represents a good estimate for the required pulse parameters necessary to run this experiment.
To make this technique even more interesting to metrology, nanoscience, biological imaging and the next-generation lithography, the overall performance has to be pushed further, especially the resolution. Larger detectors would be capable of capturing higher spatial frequencies. A similar effect can be obtained with a smaller pixel size camera and, at the same time, a reduced sample to CCD distance. A second possibility is to use shorter wavelength sources. A third approach is to reduce the spectral bandwidth using either narrower band mirrors or by decreasing the harmonic bandwidth, e.g. with pulse shaping techniques.

However, even pushing the resolution does not help to solve a severe issue of this process, the low conversion efficiency inherent in HHG. Since the integration time for the diffraction pattern depends on both the conversion efficiency and the repetition rate of the driving laser source an increased repetition rate would have astonishing effects. In this experiment the longest integration time with a 3 kHz source is 2 hours, so already a factor of 10 would result in a 12 minute measurement. Unfortunately, state-of-the-art Ti:Sapphire amplifiers are limited to tens of kHz, because of thermo-optical issues.
The second part of this work gives a detailed investigation of an OPCPA system that could help to solve this problem in the future (chapter 6) subject to the condition that the required intensities for HHG can be achieved.

Chapter 3

Fiber laser and amplifier

First investigated by Shawlow and Townes in 1958 [1] and demonstrated by Maiman in 1960 [2] the Laser opened the door for a completely new scientific field. A lot of applications have been found to date that also affect our daily life in an impressive manner, such as laser scanner in stores, CD and DVD drives, telephone and internet, just to mention some.
As early as 1964 Koester and Snitzer [45] demonstrated the first fiber laser, but it did not draw a lot of attention. With the rapid development in optical telecommunication technology especially Erbium-doped fiber lasers and amplifiers were issues of intense research and engineering. Due to the immense progress in fiber design, the availability of pump lasers and the outstanding thermo-optical properties of fibers, the efforts in this research area were rising since the beginning of the 1990s.
This section provides a brief outline of the development of fiber design, lasers and amplifiers, while emphasis is put on Ytterbium-doped amplifiers, since they are extensively used in this work.

3.1 Design and advantages of fiber lasers

Most solid-state lasers suffer from thermal problems arising from thermal lensing or thermal birefringence in the laser medium, which considerably affect the beam quality. Due to the large ratio of surface-to-active volume of a fiber the heat load is distributed over a long length [20]. Thats why they are almost immune against thermo-optical problems so that the beam quality basically depends on the design of the fiber itself.

3.1.1 Optical Fibers as waveguides

The simplest fiber design one can imagine is a core surrounded by a cladding whose refractive index is lower (Step Index Fiber, fig. 3.1). To protect the fiber there is a polymer jacket.

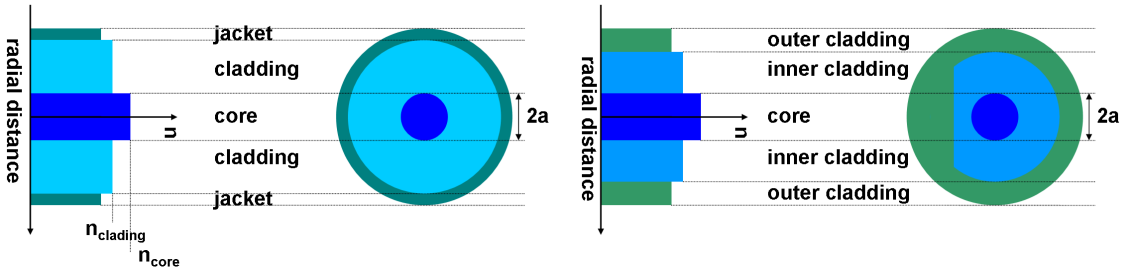

Figure 3.1: Fiber Designs. *Left Side*: Architecture of a simple Step Index Fiber (SIF). The core is surrounded by a lower index cladding and a protective coating (jacket). *Right Side*: Architecture of a Double Clad Fiber. The singlemode active core is surrounded by a multimode D-shaped pump core providing efficient pump light incoupling.

The light is guided in the core by total internal reflection. To build a laser, the core is doped by rare-earth ions, e.g. Yb^{3+}, Nd^{3+} or Er^{3+}, and dieletric mirrors are put on the ends of the fiber making the whole setup very compact and stable.
The waveguide structure of a fiber not just guides the laser radiation, but also the pump light. So a high gain can be achieved due to the long interaction length, resulting in a low pump threshold. The transverse mode structure is basically determined by the refractive index profile of a fiber. For a simple Step Index Fiber (SIF) the V Parameter describes the mode-guiding properties of a fiber. It is found to be [46]

$$V = \frac{2\pi}{\lambda} a \sqrt{n_{core}^2 - n_{cladding}^2}, \tag{3.1}$$

where λ is the wavelength, a is the core radius, n_{core} is the refractive index of the core and $n_{cladding}$ is the refractive index of the cladding, respectively. For $V < 2.405$ the fiber is said to be singlemode only guiding the LP_{01}-Mode. Naturally, this condition also limits the wavelength range for single mode operation, since the fiber design (n_{core}, $n_{cladding}$, a) is fixed. Some mode profiles can be seen in figure 3.2 simulated for a slightly multimode fiber ($V = 2.38$) with a simple finite difference approximation to solve the scalar Helmholtz equation [48].

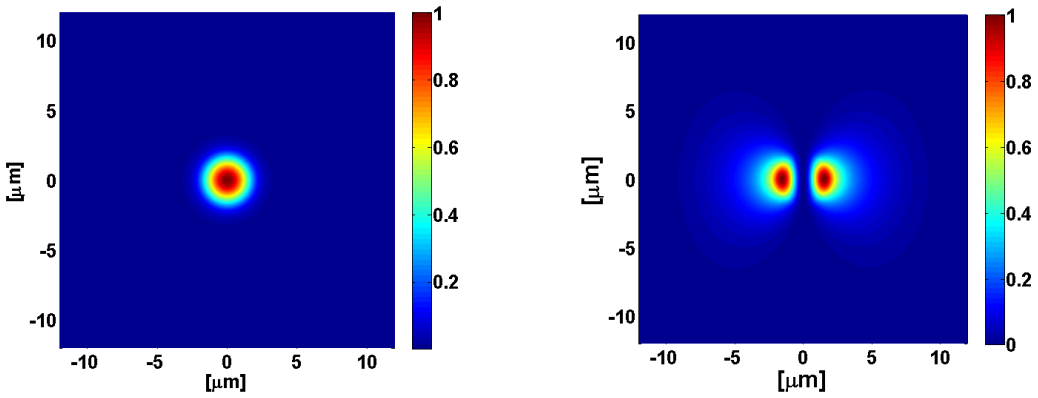

(a) LP_{01} mode of SIF with V=2.38.

(b) LP_{11} mode of SIF with V=2.38.

Figure 3.2: Modes of a fiber simulated with the help of a simple finite difference approximation of the Scalar Helmoltz equation.

Fiber lasers based on single cladding fibers are limited in output power due to the availability of singlemode pump diodes. The laser has to be operated in a singlemode regime in order to suppress energy transfer to higher order modes, but the pump diodes are limited to a few Watts of output power in singlemode operation. This drawback could be overcome by modifying the fiber design. Adding a multimode pumpcore around the singlemode core has the capability to couple low brightness high power diode lasers. Additionally, breaking the cylindrical symmetry (fig. 3.1) leads to more efficient pump light absorption [47]. The performance of this fiber concept is mainly limited by nonlinear effects, such as Self Phase Modulation (SPM), Stimulated Raman Scattering (SRS) or Stimulated Brillouin Scattering (SBS). They arise due to the long interaction length and strong confinement in fibers and are significant for pulsed and CW operation as well. Large Mode Area (LMA) fibers helped to push the output powers even higher, but the accuracy of $\Delta n = n_{core} - n_{cladding}$ can only be ensured within 10^{-3}, and therefore, limits the core dimensions in single mode operation.
To further increase the active core size while maintaining singlemode operation, a completely new approach of microstructuring optical fibers has been proposed. The simplest "one missing hole" design consists of a triangular array of air holes with diameter d and pitch Λ forming the cladding (fig. 3.3). Obviously, the air holes and the glass matrix form a kind of average refractive index in the cladding that is lower than the core refractive index leading to the waveguide properties already discussed above. Due to their structure these fibers are called Photonic Crystal Fibers (PCF). Variation of the quantities λ/Λ and

d/Λ determines the properties, such as number of guided modes, dispersion or birefringence [49]. For $d/\Lambda < 0.45$ "one missing hole" PCF are said to be endlessly single mode, theoretically making it possible to create arbitrarily large cores. Mode-field-diameters of more than 20 μm became possible, but naturally the core size is limited by other mechanisms, i.e. higher propagation losses. Further improvements include new arrangements of the air holes and also increasing the number of missing holes to 3,7 and 19 resulting in even larger cores (up to 100 μm in so called Rod-type fibers, [50]). The double clad concept has been adapted to photonic crystal fibers as well. High NA pump cores can be fabricated with the "air-clad" technology [51]. An additional ring of air holes around the pump core is used to guide light with a high beam parameter product (BPP)[1].

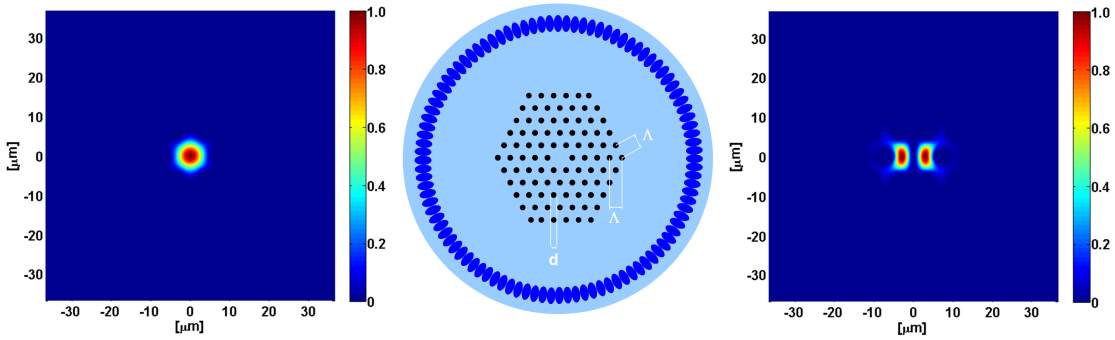

Figure 3.3: Transverse profile of a "one missing hole" design Photonic Crystal Fiber with air-clad (middle) and corresponding transversal mode-fields LP_{01} (left) and LP_{11} (right) for a fiber with $d/\lambda = 0.5$ and $\lambda/\Lambda = 0.15$.

3.2 Amplifiers based on Ytterbium-doped fibers

The first laser operation in Ytterbium-activated silicate glass was observed by Etzel *et. al* [52] in 1962. But due to the rapid progress in Nd^{3+} doped laser materials it attracted only little interest for a while [53]. Even fiber technology was dominated by Erbium-doped fiber amplifiers, because of their extensive use in optical communication technique. Ytterbium itself attracted attention with growing interest in the amplification of pulses to provide a source of very high peak powers [24].
Ytterbium based fiber amplifiers offer some advantageous characteristics, i.e. a broad absorption (860 nm - 1064 nm) and emission bandwidth (975 nm - 1200 nm) (fig. 3.4) and

[1]The BPP is the product of the beams divergence half-angle (in mrad) and the spot size (in mm).

excellent conversion efficiency due to the low quantum defect and high gain owing to the possibility of high doping levels.

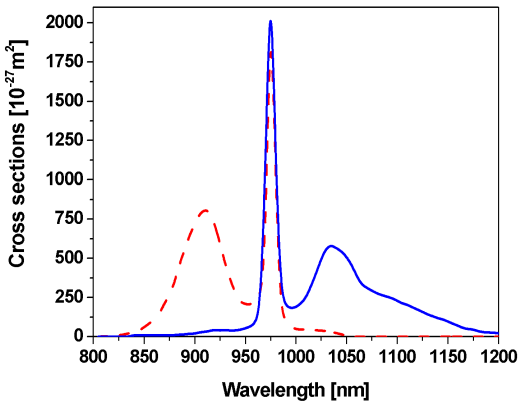

Figure 3.4: Absorption (red dashed line) and emission (blue line) cross-section of Ytterbium in silicate glass (from [24]).

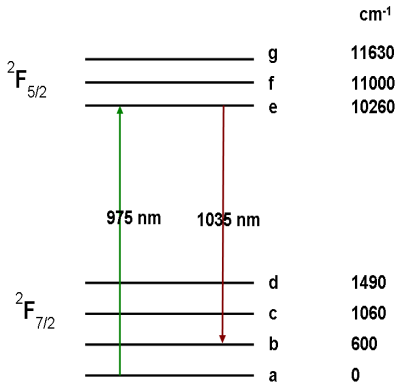

Figure 3.5: Energy level structure of Yb^{3+} in silica with the corresponding energies and transitions [53].

The electronic structure of the Yb^{3+}-ion provides only three level and quasi-three level transitions. The energy level structure consists of two manifolds, the $^2F_{7/2}$ ground state with four Stark levels and the $^2F_{5/2}$ excited state with three Stark levels (fig.3.5). Advantageously, there is no Excited State Absorption (ESA)[2] and due to the large gap no nonradiative decays via multiphonon emission and concentration quenching occur [53]. Fiber amplifier systems, based on Ytterbium doping, presented in this work were operated with 975 nm pump wavelength and 1030 nm signal wavelength. A look at the emission- and absorption cross sections in figure 3.4 shows an absorption (and also an emission) peak at 975 nm and an emission peak at 1030 nm. The peak at 975 nm corresponds to transitions between the lowest Stark levels in each manifold while the emission at 1030 nm is linked with the transitions from level e to b (fig. 3.5). A more detailed analysis of spectroscopic properties, gain calculation and laser regimes can be found in [53] and [24] and is beyond the scope of this work.

[2]ESA: the phenomenon that light is absorbed by ions or atoms in an excited state, rather than in the electronic ground state [54]

Chapter 4

Pulse propagation in fibers

The preceding section described guiding properties of fibers as optical waveguides. Naturally, these characteristics will depend on the wavelength of the propagating light wave, and therefore, can be an severe issue for short light pulses. They are composed of a broad frequency spectrum, since their time and frequency domain are connected via Fourier transform and obey an uncertainty relation

$$\Delta\tau \cdot \Delta\nu \geq \text{const.}, \tag{4.1}$$

where $\Delta\tau$ is the pulse duration (FWHM), $\Delta\nu$ the spectral width (FWHM) and the equal sign belongs to a transform limited pulse. Propagating through materials seriously changes properties of light pulses owing to an effect called dispersion. Due to the strong confinement, fibers suffer from another limitation, namely nonlinear effects (see also 5). Interestingly the interplay of dispersion and nonlinearity can lead to great variety of effects that can be beneficial. The generation of a fundamental soliton that does not change its temporal shape during propagation is one of these effects investigated in this work.
This chapter is supposed to introduce the phenomenon of dispersion and how it affects propagation. Furthermore it is shown what can be done to effectively use dispersion and nonlinearity to control the propagation of short light pulses by the means of soliton generation.

4.1 Dispersion

When light travels through an arbitrary medium it will see the frequency dependent susceptibility, refractive index and speed of light, what is referred to as dispersion [59]. A short pulse (with a broad frequency spectrum, eq. 4.1) will change its temporal shape due

to the resulting frequency dependence of the phase and group velocity. For the duration Δt of an optical pulse the following expression can be found [56]

$$\Delta t^2 = \int \left| \frac{\partial \rho(\omega)}{\partial \omega} \right|^2 d\omega + \int \left| \rho(\omega) \frac{\partial \Phi}{\partial \omega} \right|^2 d\omega, \tag{4.2}$$

where the electrical field is described by $E(\omega) = \rho(\omega) e^{i\Phi_0(\omega)}$ and $\Phi(\omega) = \Phi_0(\omega) + \omega\langle t \rangle$. This expression shows that only pulses with a flat phase ($\partial\Phi/\partial\omega = 0$ over the entire spectrum) have the shortest duration and are considered as transform limited. To describe basic dispersive properties of materials the spectral phase is approximated by a Taylor expansion

$$\Phi(\omega) = \sum_n \frac{1}{n!} \left. \frac{\partial^n \Phi}{\partial \omega^n} \right|_{\omega_0} (\omega - \omega_0)^n. \tag{4.3}$$

The n-th derivative of the phase function with respect to the frequency is often specified in units of [fs^n] and has a particular physical meaning. The zeroth order $\Phi^0(\omega_0)$ is called absolute phase, i.e. the phase accumulated by the reference frequency ω_0. The time $\Phi^1(\omega_0)$ for a wave packet centered at the reference frequency to propagate between two reference planes is called group delay. Both of them are not considered in the analysis of dispersive systems, since they do not affect the pulse duration. The first important term is the group delay dispersion (GDD) $\Phi^2(\omega_0)$ that directly leads to pulse broadening and a time dependent instantaneous frequency, termed “chirp”. For the propagation in fibers it is more common to speak of propagation constants $\beta(\omega)$ connected with the phase via

$$\Phi(\omega) = \beta(\omega) \cdot L, \tag{4.4}$$

where L is the propagation length in the fiber. The second order dispersion is then read as $\beta_2 = \frac{\Phi^2(\omega_0)}{L}$. In fiber optics the more common D-Parameter is

$$D(\lambda) = -\frac{2\pi c}{\lambda^2} \beta_2, \tag{4.5}$$

specified in $[\mathrm{D}] = 1\mathrm{ps}/(\mathrm{nm} \cdot \mathrm{km})$. For normal dispersion ($\beta_2 > 0$) the parameter D is negative while it is positive for anomalous dispersion ($\beta_2 < 0$).
For ultrashort pulses even higher order dispersion, e.g. $\Phi^3(\omega_0)$ or $\Phi^4(\omega_0)$, has to be considered. For the generation of the shortest pulses a very careful dispersion analysis and compensation is inevitable.

4.1.1 Chirped Pulse Amplification - CPA

Despite the detrimental effects of dispersion to ultrashort pulses it can be a very useful tool for amplifying them. Originally established in radar Strickland and Mourou [57] demonstrated the technique of Chirped Pulse Amplification (CPA) in the optical regime. A short, low-energy pulse is temporally stretched by the means of a dispersive element, therefore reducing the peak power. Consequently, distortions due to nonlinear effects are reduced and damage of the medium is prevented. Due to the lowered peak power, these pulses can be amplified to much higher energy levels. Finally, a second dispersive element with contrarily characteristics re-compresses the pulse resulting in a high energy pulse with a short pulse duration (fig. 4.1). Even though new techniques have been investigated CPA is a widely used state-of-the-art technology.

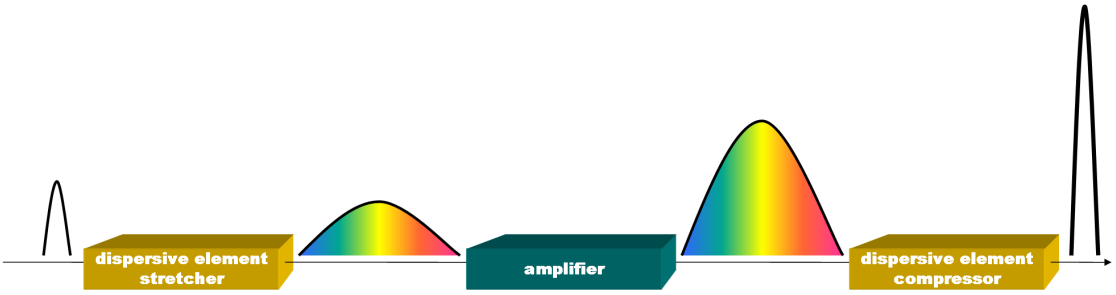

Figure 4.1: CPA: After stretching a pulse temporally it is amplified and re-compressed by a dispersive element with opposite dispersion characteristics.

4.1.2 Stretcher and Compressor

For the realization of a CPA system materials or setups that provide certain dispersion properties are necessary. Since there are three major physical origins of dispersion [56], namely material dispersion (refractive index depends on frequency), interference and geometrical dispersion (different optical path lengths for every frequency component), one can think of a great variety of possibilities how to disperse optical pulses. The easiest way to stretch an unchirped pulse is to propagate it through a material, e.g. a block of fused silica glass. More sophisticated tools are prism or grating compressors and grating stretchers that are the basic tools in today's CPA systems. Especially combinations of grating stretcher and compressor are very interesting since their dispersion properties match perfectly. More recently a new type of mirror, called Chirped Multilayer Mirror [58], relying

on interference has attracted attention due to tailorable dispersion characteristics.

4.2 Soliton generation

Even though nonlinear effects are discussed in chapter 5 some are mentioned here in order to describe soliton effects in fibers. Equation 5.1 describes the nonlinear response of some media exposed to electrical fields. Since $\chi^{(2)}$ vanishes for materials with inversion symmetry, the lowest order nonlinear effects in fused silica fibers are the third order ones induced by $\chi^{(3)}$. Without efforts to enhance processes like third-harmonic generation and four-wave-mixing the most dominant effects arise from the intensity dependence of the refractive index. Others, not discussed in detail, are cross-phase modulation (XPM), stimulated Raman scattering (SRS) and stimulated Brillouin Scattering (SBS).

4.2.1 Self-Phase-Modulation - SPM

The intensity dependent refractive index can be found to be [46]

$$\tilde{n} = n + n_2 \cdot |E|^2, \tag{4.6}$$

where n is the linear index and the nonlinear-index coefficient is related to $\chi^{(3)}$ via

$$n_2 = \frac{3}{8n}\Re(\chi^3_{xxxx}) \tag{4.7}$$

for a linearly polarized field, where $\Re(\chi^3_{xxxx})$ is the contributing component of the $\chi^{(3)}$-tensor. It is more common to write the intensity I instead of $|E|^2$ in equation 4.6, so that n_2 is given in $[m^2/W]$ with typical values of 2.2...3.4·10^{-2} m^2/W in silica glass [46]. This nonlinear index of refraction induces a intensity-dependent phase shift Φ_{NL} referred to as self-phase modulation (SPM). A normalized amplitude U(z,T) changes after propagating through a fiber of length L by [46]

$$\mathrm{U(L,T)} = \mathrm{U(0,T)} \cdot \exp(i \cdot \Phi_{NL}(L,T)), \tag{4.8}$$

where $\Phi_{NL}(L,T) = |\mathrm{U(0,T)}|^2 (\mathrm{L}_{eff})/\mathrm{L}_{NL})$ is the nonlinear phase shift. The nonlinear length L_{NL} is given by $\mathrm{L}_{NL} = (\gamma \mathrm{P}_0)^{-1}$, where P_0 is the peak power and γ the nonlinear parameter related to n_2 by

$$\gamma = \frac{n_2 \cdot \omega_0}{c \cdot A_{eff}} \tag{4.9}$$

with the effective mode field area A_{eff} [1]. $L_{eff} = [1-\exp(-\alpha L)]/\alpha$ is the effective length for a pulse that also accounts for fiber losses (α<0) or gain (α>0). Speaking of short pulses, it is clear that the intensity and, hence, the nonlinear phase (eq. 4.8) is a function of time resulting in a spectral broadening. The instantaneous frequency differs across the pulse from its central frequency ω_0 by

$$\delta\omega(T) = -\frac{\partial\Phi_{NL}}{\partial T} = -\left(\frac{L_{eff}}{L_{NL}}\right)\frac{\partial}{\partial T}|U(0,T)|^2 \tag{4.10}$$

inducing a chirp. As the pulse propagates through the fiber new frequency components are continuously added depending on its temporal pulse shape.

4.2.2 Combined effects of dispersion and SPM

The preceding sections described the effects of dispersion and SPM on short pulses independently. A consideration of both leads to a new phenomenon known as soliton, a wave packet that does not change its shape during propagation.
Mathematically the pulse propagation in fibers is described by the nonlinear Schrödinger equation (NLSE) that accounts for dispersion, nonlinearity, losses and gain. A simple approximation just considering second order dispersion and SPM reads as

$$\frac{\partial A}{\partial z} = -i\frac{\beta_2}{2}\frac{\partial^2}{\partial T^2}A + i\gamma|A|^2A, \tag{4.11}$$

where A is the slowly varying envelope [59]. For different signs of β_2 and γ, namely in the anomalous dispersion region (since $\gamma > 0$), a special soliton solution is found to be [46]

$$A(z,T) = \sqrt{P_0}\cdot sech\left(\frac{T}{T_0}\right)\cdot e^{i\frac{z}{2L_D}}, \tag{4.12}$$

where P_0 is the initial peak power, T_0 the 1/e intensity width and $L_D = T_0^2/|\beta_2|$ the dispersion length, respectively. The soliton order N is determined by

$$N^2 = \frac{L_D}{L_{NL}} = \frac{\gamma\cdot P_0\cdot T_0^2}{|\beta_2|}. \tag{4.13}$$

Descriptively, the soliton effect can be understood as follows: In the anomalous dispersion regime the blue spectral components travel faster than the red ones, while it is vice versa

[1] The effective mode field area is basically determined by the guiding and design properties of the fiber, since it can be found to be $\left(\int\int_{-\infty}^{\infty}|F(x,y)|^2dxdy\right)^2 / \int\int_{-\infty}^{\infty}|F(x,y)|^4dxdy$ for the transverse mode structure $F(x,y)$.

for SPM, resulting in a stable solution.
Only the fundamental soliton with N=1 will propagate without spectral and temporal changes. The jth order solitons (N=j) consist of j fundamental solitons with peak powers P_j and pulse durations T_j [60]

$$P_j = \frac{(2N-2j+1)^2}{N^2} P_0 \quad \text{and} \quad T_j = \frac{T_0}{2N-2j+1}. \tag{4.14}$$

In the absence of perturbations they travel with the same group velocity and, hence, they interfere with each other so that they have a periodical spectral and temporal evolution (fig. 4.2).

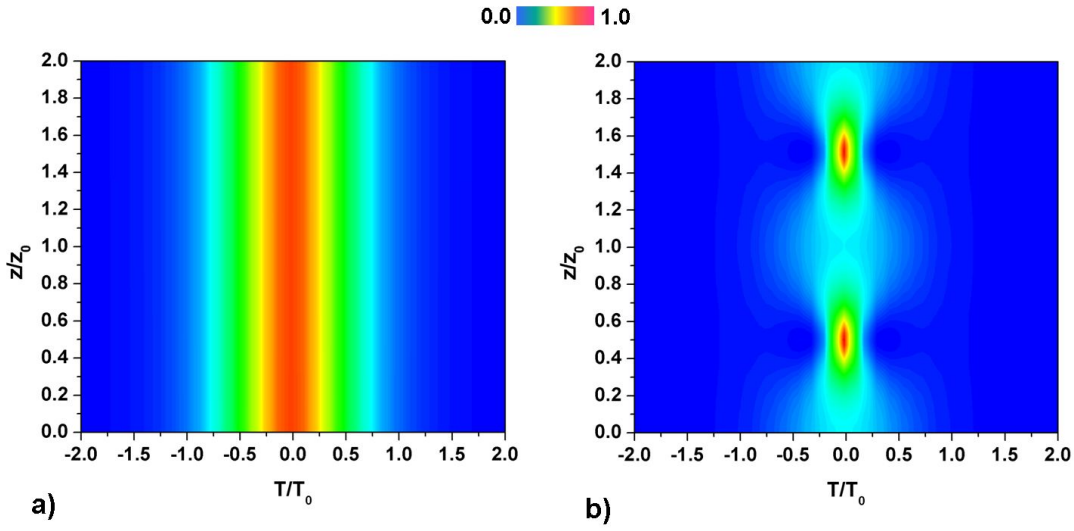

Figure 4.2: Temporal evolution of a soliton with order N=1 (a) and N=2 (b) over two soliton periods.

After a period of $z_0 = \pi/2 \cdot L_D$ they are reshaped. The presence of perturbations, though, can disturb the propagation of solitons, e.g. third order dispersion leads to the generation of resonant dispersive waves. Also nonlinear effects like self-steepening (soliton decays into its constituents) and Raman scattering (soliton self-frequency-shift) have to be taken into account.
Self-Steepening originates from the intensity dependence of the group velocity and leads to an asymmetry in the SPM-broadened spectra, especially of ultrashort pulses. Since the peak is evolving slower than the wings, it shifts toward the trailing edge.

The Raman scattering is an inelastic and non-instantaneous scattering process caused by vibrations of the glass molecules, which are associated with optical phonons. An incident photon can be annihilated and a phonon and a new photon at lower frequency can be created. Therefore, energy is transferred to longer wavelengths and becomes apparent as a wavelength shift in the spectrum which is maximized for a shift of 13 THz in fused silica. The Raman threshold for a fiber with the effective length L_{eff} and the mode field area A is found to be [46]

$$P_{Th}^{Ra} \approx 16 \frac{A}{g_R L_{eff}}, \tag{4.15}$$

where g_R is the Raman gain coefficient.

Chapter 5

Parametric frequency conversion

Almost simultaneous with the invention of the laser [2] nonlinear optical effects have been discovered [10] and investigated [61]. Phenomena in nature that we can observe in our daily life are dictated by linear optics, where optical properties do not depend on the intensity of illumination. However, if sufficiently high intensities of light propagate through materials extraordinary effects arise due to the fact that waves start to interact with others, e.g. the generation of the second harmonic, sum- or difference frequency generation and self focussing.
The intention of the following chapter is to give a brief introduction to nonlinear optics and its phenomena. After describing the basics the most important nonlinear effects that are investigated or used in this work are introduced while emphasis is put on the process of parametric amplification.

5.1 Optical Nonlinearities

To understand nonlinear optical effects it is necessary to study the interaction of light waves with matter. Since every medium consists of charged particles, i.e. electrons and ion cores, an applied field results in an acceleration of these particles and induces a collection of electrical dipoles, in other words a polarization [62]. Due to the high optical frequencies (10^{13} Hz to 10^{17} Hz) these dipoles oscillate and the core movement can be neglected so that just the electrons have to be considered. A simple mechanical analog is to think of an electron attached to the core by a spring. For weak fields the displacement of the electron will be small resulting in a linear response, because the electron moves in a parabolic potential, hence, behaving like a harmonic oscillator. With increasing field strength the electron moves further away from its ionic core so that it sees a non-parabolic

potential. The main consequence is that the response gets nonlinear and the dipoles can start oscillating at frequencies of 2ω, 3ω and so on. Since oscillating dipoles radiate, new frequency components are created.
To develop a pratical model it turned out to be useful to expand the polarization in a power series

$$P = \varepsilon_0(\chi^{(1)}E + \chi^{(2)}E^2 + \chi^{(3)}E^3 + ...), \tag{5.1}$$

where $\chi^{(1)}$ is the linear and $\chi^{(2)}$ and $\chi^{(3)}$ are the nonlinear susceptibilities, respectively [62]. According to the power of the electrical field in equation 5.1 nonlinear effects are classified. Effects arising from $\chi^{(2)}$ are called second order nonlinear effects, e.g. second harmonic generation, while third order nonlinear effects such as self phase modulation arise from $\chi^{(3)}$ (see chapter 4).

5.1.1 Coupled Waves

The polarization in equation 5.1 is the driving quantity for nonlinear phenomena. The governing wave equation for propagating vector electrical fields is directly derived from Maxwell's equations [63], [64]

$$\left[\nabla \times (\nabla \times) + \frac{1}{c^2}\frac{\partial^2}{\partial t^2}\right]\vec{E}(\vec{r},t) = -\frac{1}{\varepsilon_0 c^2}\frac{\partial^2}{\partial t^2}\vec{P}(\vec{r},t), \tag{5.2}$$

where c is the speed of light, ε_0 the dielectric constant of vacuum, $\vec{E}(\vec{r},t)$ the electrical field and $\vec{P}(\vec{r},t)$ the polarization, respectively. A decomposition of the vector fields into a set of plane waves and the transformation of the wave equation 5.2 into frequency domain reveals a set of coupled wave equations

$$\left[\nabla \times (\nabla \times) - \frac{\omega^2}{c^2}\boldsymbol{\varepsilon}\cdot\right]\vec{E}(\vec{k}_m, w) = \frac{\omega^2}{\varepsilon_0 c^2}\vec{P}^{NL}(\vec{k}_m, \omega_m = \omega). \tag{5.3}$$

For n interacting waves there are (n+1) differential equations describing the interaction coupled by the nonlinear polarization. For practical purposes the propagating electrical field is written as

$$\vec{E}(\omega, z) = \Re(A(z)e^{i(kz-\omega t)}), \tag{5.4}$$

with the envelope $A(z)$. For a significant energy transfer the wave has to travel a distance much longer than its wavelength, thus,

$$\left|\frac{\partial^2 A}{\partial z^2}\right| \ll \left|k\frac{\partial A}{\partial z}\right| \tag{5.5}$$

is valid and called slowly varying envelope approximation (SVEA). With the help of equation 5.5 a set of coupled wave equations for the envelopes can be found (see next section).
For all nonlinear interactions the energy is conserved

$$\frac{d}{dz}\sum_{\mu=1}^{m+1} I_\mu = 0 \tag{5.6}$$

and remains in the form of electromagnetic energy, while energy can flow between the particular waves, thus, this process is called parametric [1]. Additionally, for each frequency ω_μ the condition

$$\frac{d}{dz}\left(\frac{I_{m+1}}{\omega_{m+1}} \pm \frac{I_\mu}{\omega_\mu}\right) = 0 \tag{5.7}$$

holds, where the sign corresponds to that of ω_μ in the susceptibility tensor [2]. Equation 5.7 says that for the creation of a photon at ω_{m+1} a photon at ω_μ is created (-) or destroyed (+). The relations 5.6 and 5.7 are known as Manley-Rowe relations [66]. For the most efficient energy transfer also the momentum conservation has to be fulfilled. This situation is referred to as phase matching and will play an important role in all the nonlinear phenomena investigated in this work.

5.2 Second Harmonic Generation

A particular second order nonlinear process is the second harmonic generation, which was the first ever to be observed [10]. It is the degeneration of sum frequency generation (SFG) where two incident photons with ω_1 and ω_2 create a photon with $\omega_3 = \omega_1 + \omega_2$, for $\omega_1 = \omega_2$ we speak of second harmonic generation. The coupled wave equations can be found to be [64]

$$\begin{aligned}\frac{dA_\omega}{dz} &= i\frac{2\omega}{n_\omega c} d_{eff} A_\omega^* A_{2\omega} e^{-i\Delta k z} \\ \frac{dA_{2\omega}}{dz} &= i\frac{2\omega}{n_{2\omega} c} d_{eff} A_\omega^2 e^{i\Delta k z},\end{aligned} \tag{5.8}$$

[1] I_μ is the intensity of the wave $\mu = 1 \ldots m+1$

[2] A more detailed study of the polarization reveals the properties of the susceptibility tensor χ and how frequencies can be mixed. Basically negative frequencies belong to difference frequency generation [65]

where d_{eff} is the effective nonlinear coefficient that accounts for direction of propagation, polarization and crystal orientation, n_ω and $n_{2\omega}$ are the refractive indices of the fundamental and second harmonic, $\Delta k = 2k_\omega - k_{2\omega}$ is the phase mismatch, respectively. For the undepleted-pump approximation and perfect phase matching, i.e. $\Delta k = 0$, an analytic solution can be found [67], [61]

$$I_\omega(z) = I_\omega(0) sech(z/l) \tag{5.9}$$

$$I_{2\omega}(z) = I_\omega(0) \tanh^2(z/l) \tag{5.10}$$

$$l = \frac{1}{4\pi d_{eff}} \sqrt{\frac{2\varepsilon_0 n_\omega^2 n_{2\omega} c \lambda_\omega^2}{I_\omega(0)}}. \tag{5.11}$$

For high conversion efficiencies the pump depletion can not be neglected any more, so that numerical approaches have to be performed in order to find solutions of the coupled wave equations.
Naturally, the energy transfer gets less efficient for $\Delta k \neq 0$, because this phase mismatch means that the microscopic dipoles radiating at ω and 2ω are dephased and, hence, the signal can not build up coherently. For $\Delta k \cdot L = 2\pi$ they are completely out of phase. The corresponding length $L_c = 2\pi/\Delta k$ is called coherent buildup length of interaction [67].
Hence, to efficiently convert energy from the fundamental to the second harmonic wave phase matching has to be achieved. For second harmonic generation the condition $2k_\omega = k_{2\omega}$ can be expressed as

$$n(\omega) = n(2\omega). \tag{5.12}$$

Normal dispersive media do not provide a possibility for phase matching, but birefringent media do, because the index of refraction depends on the polarization of the light waves. Generally, there are two types of phase matching. TypeI is the case were the lower frequencies have the same polarization while TypeII is achieved when the two lower frequency waves are orthogonally polarized [3].
For an ordinary polarized fundamental and an extraordinary polarized second harmonic wave phase matching can be achieved for a specific angle θ_{pm} with respect to the optical axis (fig. 5.1). For uniaxial crystals with ordinary index n^o and extraordinary index n^{eo} the phase matching angle θ_{pm} for the above mentioned polarization is [64]

$$\theta_{pm} = \arcsin \left[\frac{n_{2\omega}^e}{n_\omega^o} \sqrt{\left[\frac{(n_{2\omega}^o)^2 - (n_\omega^o)^2}{(n_{2\omega}^o)^2 - (n_{2\omega}^e)^2} \right]} \right]. \tag{5.13}$$

[3] Note that SHG is the degeneration of sum frequency generation (SFG) so that the lower frequencies are the two photons of the fundamental wave

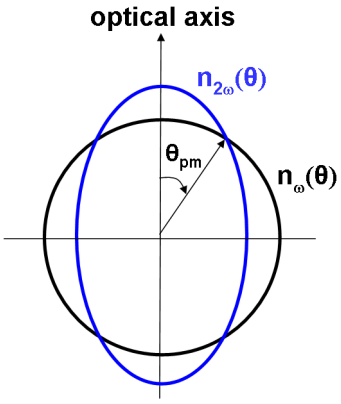

Figure 5.1: Phase matching for second harmonic generation.

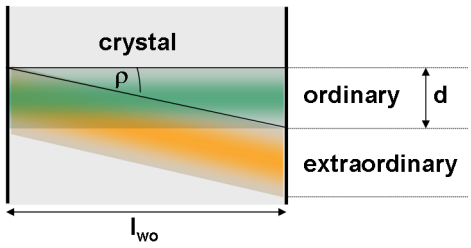

Figure 5.2: Schematic illustration of the spatial walk off. The extraordinary and ordinary beams separate after a walk-off length l_{wo}.

A main drawback of this approach is the walk off. Since the Poynting vector and the propagation vector are not parallel for extraordinary polarized waves (except for $\theta = 0°, 90°$) ordinary and extraordinary wave diverge from each other while propagating through the crystal (fig.5.2). The walk off angle ρ for uniaxial crystals is given by [64]

$$\tan(\rho) = \frac{[n^e(\theta)]^2}{2}\left[\frac{1}{(n^e)^2} - \frac{1}{(n^o)^2}\right]\sin(2\theta) \tag{5.14}$$

leading to a spatial walk-off length of

$$l_{wo} = \frac{d}{\tan(\rho)} \tag{5.15}$$

for beams with diameter d. Other possibilities of phase matching are tuning the temperature of the crystal or periodically poling it, what is referred to as quasi phase matching (QPM).

5.3 Parametric amplification

In section 5.2 the process of SHG was already described as degenerated sum frequency generation. Another process, well known in nonlinear optics, is the difference frequency

generation (DFG) where a strong pump beam with ω_p can amplify a weak signal beam with ω_s (ω_s<ω_p). Energy conservation $\hbar\omega_p = \hbar\omega_s + \hbar\omega_i$ predicts the creation of an idler beam with $\omega_i = \omega_p - \omega_i$, so that $\omega_i < \omega_s < \omega_p$. For efficient energy transfer, of course, the conservation of momentum $\hbar\vec{k}_p = \hbar\vec{k}_s + \hbar\vec{k}_i$ is essential. To observe this effect intensities on the order of tens of GW/cm^2 are required [68], while parametric frequency conversion can also be obtained in CW operation with the help of quasi phase matching (QPM), that for example can be obtained in periodically poled Lithium Niobate (PPLN) [69].
There are two ways to exploit this nonlinear process. Enclosing the crystal in a cavity can lead to an optical parametric oscillator (OPO) when the parametric gain exceeds the losses. Output energies of these devices are typically low (few nJ) and the cavity length has to be matched with the pump laser quite excatly ($\approx \mu m$). Another approach is to amplify a weak "seed" beam, what is referred to as optical parametric amplification (OPA) and can provide high output energy and broad frequency tunability (UV - mid IR). The shortest pulses in the visible with a duration of 4 fs have been created with an OPA [25].

5.3.1 Optical parametric amplifier - OPA

For parametric amplification a set of coupled wave equations can be found for the slowly varying envelopes as well

$$\begin{aligned}
\frac{dA_i}{dz} &= i\frac{\omega_i d_{eff}}{n_i c} A_s^* A_p e^{i\Delta kz}, \\
\frac{dA_s}{dz} &= i\frac{\omega_s d_{eff}}{n_s c} A_i^* A_p e^{i\Delta kz}, \\
\frac{dA_p}{dz} &= i\frac{\omega_p d_{eff}}{n_p c} A_i A_s e^{-i\Delta kz},
\end{aligned} \tag{5.16}$$

where $\Delta k = k_p - k_i - k_s$ is the collinear wave-number mismatch. For negligible pump depletion ($A_p \approx$ const.) an analytical solution for a crystal of length L is

$$I_s(L) = I_{s0}\left[1 + \frac{\Gamma^2}{g^2}\sinh^2(gL)\right], \tag{5.17}$$

$$I_i(L) = I_{s0}\frac{\omega_i}{\omega_s}\frac{\Gamma^2}{g^2}\sinh^2(gL), \tag{5.18}$$

where the gain g and the parameter Γ can be expressed as

$$g = \sqrt{\Gamma^2 - \left(\frac{\Delta k}{2}\right)^2}, \tag{5.19}$$

$$\Gamma^2 = \frac{2\omega_i \omega_s d_{eff}^2 I_p}{n_i n_s n_p \varepsilon_0 c_0^3}. \tag{5.20}$$

As was the case for SHG, the condition of phase matching can be expressed in terms of the refractive indices as follows

$$n_p = \frac{n_i \omega_i + n_s \omega_s}{\omega_p}. \tag{5.21}$$

Again it can be met with a birefringent negative uniaxial crystal ($n_{eo} < n_o$) in TypeI ($o_s + o_i \rightarrow eo_p$) or TypeII ($eo_s + o_i \rightarrow eo_p$ or $o_s + eo_i \rightarrow eo_p$) phase matching while temperature tuning still remains an alternative. The phase matching angle θ_{pm} can be calculated by

$$\theta_{pm} = \arcsin\left[\frac{n_p^{eo}}{n_p^{eo}(\theta_m)}\sqrt{\frac{(n_p^o)^2 - (n_p^{eo}(\theta_m))^2}{(n_p^o)^2 - (n_p^{eo})^2}}\right]. \tag{5.22}$$

The preceding discussion always dealt with monochromatic, i.e. cw, beams interacting in a nonlinear crystal. For this work the amplification of ultrashort pulses is of great interest and needs to be considered as well. A main issue for ultrashort pulses is their different group velocity $v_g = d\omega/dk$ arising from dispersion in materials (section 4.1). If pulse broadening due to dispersion and third order nonlinear effects are neglected the differential equations 5.16 transform to

$$\begin{aligned}
\frac{\partial A_i}{\partial z} + \left(\frac{1}{v_{gi}} - \frac{1}{v_{gp}}\right)\frac{\partial A_i}{\partial \tau} &= i\frac{\omega_i d_{eff}}{n_i c_0} A_s^* A_p e^{-i\Delta k z}, \\
\frac{\partial A_s}{\partial z} + \left(\frac{1}{v_{gs}} - \frac{1}{v_{gp}}\right)\frac{\partial A_s}{\partial \tau} &= i\frac{\omega_s d_{eff}}{n_s c_0} A_i^* A_p e^{-i\Delta k z}, \\
\frac{\partial A_p}{\partial z} &= i\frac{\omega_p d_{eff}}{n_p c_0} A_s A_i e^{i\Delta k z},
\end{aligned} \tag{5.23}$$

where $\tau = t - z/v_{gp}$ is the reference time frame moving with the pump pulse. The coupled equations 5.23 show that there is a temporal walk-off due to group velocity mismatch

(GVM) between signal and pump (or idler and pump) limiting the interaction length to

$$l_{jp} = \frac{\tau_p}{\delta_{jp}}, \qquad j = s,i, \tag{5.24}$$

where τ_p is the pump pulse duration and $\delta_{jp} = 1/v_{gj} - 1/v_{gp}$ is the GVM between pump and signal/idler, respectively. GVM, and therefore, the interaction length are determined by the crystal type, pump wavelength and type of phase matching. The walk-off effect becomes more important for $\delta_{sp}\delta_{ip} > 0$, since idler and signal move away from the pump in the same direction while they tend to stay localized under the pump pulse for $\delta_{sp}\delta_{ip} < 0$. The GVM also affects the phase matching bandwidth $\Delta\nu$

$$\Delta\nu \cong \frac{2(2\ln 2)^{1/2}}{\pi}\left(\frac{\Gamma}{L}\right)^{1/2}\frac{1}{\left|1/v_{gs} - 1/v_{gi}\right|}, \tag{5.25}$$

where phase matching was assumed to be perfect for a given signal frequency. Above equation shows that GVM tends to decrease the bandwidth, that can be large for degeneracy ($\omega_s \to \omega_i$). Generally, the TypeI phase matching bandwidth is larger than it is for TypeII processes. The following section will describe how to increase the bandwidth further.

5.3.2 Advanced OPA design: NOPA and OPCPA systems

The quest for the shortest pulse generated by OPA systems was basically limited by the phase matching bandwidth. New setups have contributed in an impressive manner and made possible the generation of pulses in the sub-10 fs range.
An additional degree of freedom can be added by using a non-collinear geometry, where signal and pump form an angle α, while signal and idler form an angle Ω (fig.5.3). This setup is called non-collinear optical parametric amplifier (NOPA). For this geometry the phase matching condition becomes a vector equation that can be split into parallel and perpendicular components

$$\Delta k_{par} = k_p\cos(\alpha) - k_s - k_i\cos\Omega = 0. \tag{5.26}$$

$$\Delta k_{perp} = k_p\sin(\alpha) - k_i\sin(\Omega) = 0. \tag{5.27}$$

A straightforward algebraic calculation reveals the condition for broadband phase matching

$$v_{gs} = v_{gi}\cos(\Omega), \tag{5.28}$$

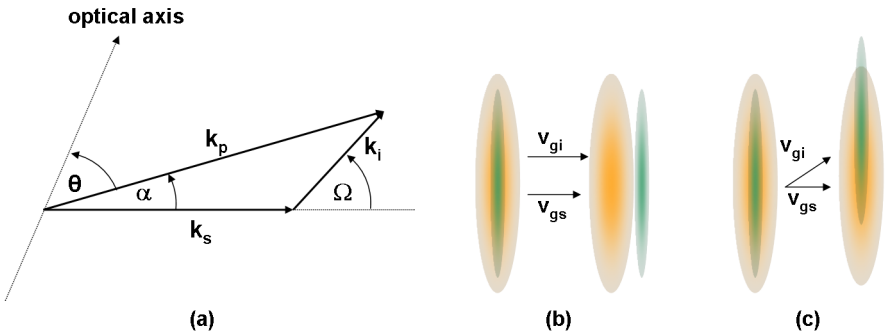

Figure 5.3: Illustration of NOPA geometry. (a) Interaction geometry for the wave vectors and corresponding angles. (b) Walk-off for signal (orange) and idler (green) in a collinear interaction geometry. (c) Walk-off for signal (orange) and idler (green) in non-collinear interaction geometry.

which shows that the signal group velocity has to equal the projection of the idler group velocity onto the signal direction. Figure 5.3 shows an intuitive understanding: For collinear interaction the signal and idler pulse start to separate quickly while they remain effectively overlapped in the phase matched non-collinear geometry. For commonly used TypeI phase matching equation 5.28 can always be met, since for negative uniaxial crystals $v_{gi} > v_{gs}$. For experimental purposes, of course, it is convenient to know the angle of the signal with respect to the pump, given by

$$\alpha = \arcsin\left(\frac{1 - v_{gs}^2/v_{gi}^2}{1 + 2v_{gs}n_s\lambda_i/v_{gi}n_i\lambda_s + n_s^2\lambda_i^2/n_i^2\lambda_s^2}\right)^{1/2}. \tag{5.29}$$

For nonlinear crystals, e.g. BBO or LBO, very broad amplification bandwidths can be achieved, when the right angle α is chosen. Figure 5.4 shows TypeI phase matching from 700 nm to 900 nm in a BBO for a pump wavelength of 518 nm and α=2.5°.
Common CPA techniques already achieved peak powers in the PW range that can only be further increased by shortening the pulses. Thus, an increased amplification bandwidth is needed, but can not be provided due to gain narrowing. To overcome this limit the NOPA seems a promising alternative and even more so when the CPA principle is adapted to parametric amplification schemes. This technique referred to as optical parametric chirped pulse amplification (OPCPA, fig. 5.5) has first been demonstrated in 1992 [70] and

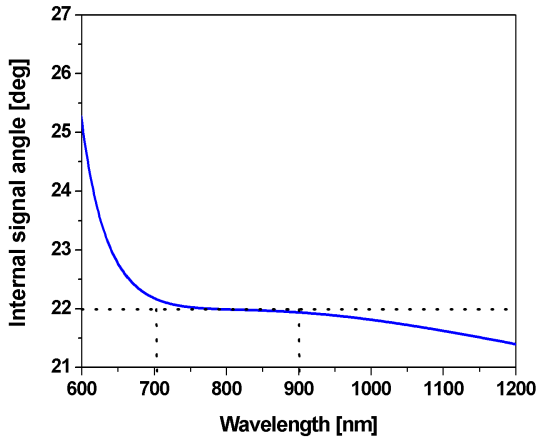

Figure 5.4: Type I phase matching in BBO. The pump wavelength is 518 nm and the internal angle between signal and pump is 2.5°.

has attracted a lot of attention over the last decade. A high energy quasimonochromatic pump pulse is coupled to a chirped low energy broadband seed pulse in a nonlinear crystal, therefore, achieving parametric gain. For sufficient stretching a high conversion over the whole bandwidth is possible resulting in very high peak power ultrashort pulses. The advantages of the OPCPA technique are high gain in short length crystals, minimal linear and nonlinear phase distortions, good temporal and spatial pulse quality and low levels of amplified spontaneous emission. Due to the energy conservation the amplification process is almost immune against thermo-optical problems, even though residual absorption can cause some thermal load, practically [68].

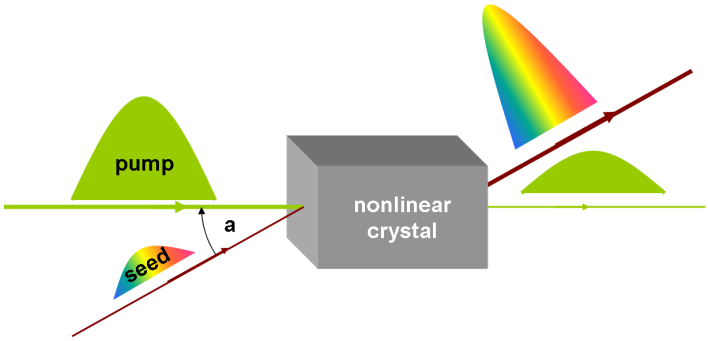

Figure 5.5: Schematic of an OPCPA system. For simplicity the idler wave is not shown.

Chapter 6

Generation of ultrashort pulses with a fiber laser pumped OPCPA system

Today's laser systems are capable of providing ultra-short and high-peak-power optical pulses igniting a stunning development ranging from industrial to scientific applications. State-of-the-art technology is based on Ti:Sapphire and limited in repetition rate to the kHz range due to thermo optical problems [71], even with advanced cooling technologies, e.g. cryogenic cooling. A main issue during the investigation of processes, initiated by high-peak-power pulses, is that they are characterized by low conversion efficiencies, e.g. high harmonic generation (chapter 2), and therefore, the detection systems have to be very sensitive. This, of course, makes real world applications almost impossible.
Diode-pumped fiber lasers offer reduced thermo-optical distortions and are therefore average power scalable while maintaining a high efficiency. Unfortunately they are not capable of providing pulses with a few 10 fs duration, since their bandwidth does not support this [24].
However, a large amplification bandwidth can be offered in optical parametric amplification, that constitutes a sophisticated technique to combine ultrashort pulse generation and amplification with high average powers. Using nonlinear crystals such as BBO or LBO and running the OPA either in a non-collinear geometry or at degeneracy provides a large amplification bandwidth (section 5.3). High gain factors (10^4 to 10^6) and short crystal lengths (only a few mm) make them suitable to generate fs pulses, since nonlinear phase distortions can be neglected. Another advantage is the already mentioned immunity to thermo-optical problems as a result of the energy conservation (chapter 5).
Femtosecond fiber laser amplification systems have been demonstrated with average power above 100 W and pulse energies of up to 1 mJ [21], [22], [23], making them a suitable pump for OPCPA systems (section 5.3).

Traditional approaches use fiber laser systems as pump and seed source for parametric amplifiers as well. A part (commonly more than 90%) of the output is frequency doubled in order to pump the device and the remainder is used to generate a continuum. With a pump radiation at approximately 515 nm the seed signal has to match the gain bandwidth (700 nm - 900 nm) of the NOPA. Common techniques to generate the white light continuum are based on two approaches: First, filamentation in bulk substrates, e.g. silica glass or Sapphire plates [26] can be used, but for a stable operation short (<100 fs) intense pulses are necessary. Second, supercontinuum generation in highly nonlinear photonic crystal fibers [27] is a stable approach. Unfortunately, both approaches, especially the fiber based technique, suffer from phase offsets inherent to the broadening process that lead to limited compressibility [72].
In this chapter a detailed investigation is presented that combines the unique properties of a Ti:Sapphire oscillator with the average power scalability of fiber amplifier systems by the means of a non-collinear optical parametric chirped pulse amplifier. The system will be described in detail and all experimental results will be presented. The front end of the presented OPCPA system is a Ti:Sapphire oscillator providing pulses at variable repetition rates. The output of this oscillator is split in order to generate seed pulses for the parametric amplification and the fiber amplifier stages as well.

6.1 Concept of high repetition rate OPCPA

The main issue of this experiment is to generate a signal pulse for the Ytterbium-doped fiber amplification stage, that has to be centered around 1030 nm. In principle, state-of-the-art broadband Ti:Sapphire oscillators based on chirped mirrors have enough bandwidth [73], but do not provide pJ energy levels (around 1030 nm) required to efficiently compete with amplified spontaneous emission. To provide the required seed, nonlinear dynamics in photonic crystal fibers are exploited. Since bulk parametric frequency converters are inefficient when directly seeded with the oscillator output, this approach provides a convenient way. The input parameters are chosen in such a way that pulses are generated at 1030 nm. These are amplified in a fiber CPA system, frequency doubled and then used as pump for the parametric amplification. The Ti:Sapphire pulses are parametrically amplified, either directly or after additional spectral broadening.
Finally, the concept is as follows: The cavity dumped Ti:Sapphire pulses are split. One portion is used to generate a pulse in the Ytterbium amplification bandwidth that is subsequently amplified, frequency doubled and used as pump source for the NOPA, while the remainder is the seed for the NOPA stage. The amplified pulses are compressed with a fused silica prism compressor to obtain ultra-short pulses.

6.2 Ti:Sapphire oscillator as front end

First demonstrated in CW operation in 1982 [74] and in ultrashort pulse operation in 1991 [75] the Ti:Sapphire oscillator has been one of the most important tools for spectroscopic purposes and a lot of other research areas in the last two decades.
The laser medium is an Al_2O_3 sapphire crystal, where a Titanium atom replaces an Aluminum atom. The Ti^{3+} ion is located in the center of a octahedron with oxygen atoms in the vertices. Due to the crystals fields the five times degenerated ground state of Ti^{3+} is split into a three times degenerated ground state ^{2}T and a twice degenerated excited state ^{2}E [76]. The Ti:Sapphire laser is considered as four level laser.
The most prominent characteristics of this type of laser are its enormous absorption (490 nm - 600 nm) and emission (670 nm - 1070 nm) bandwidths making it capable of either producing short pulses or tune it over a wide wavelength range [77]. The generation of ultrashort pulses is achieved with Kerr-Lens Modelocking (KLM).

6.2.1 Cavity-dumped Ti:Al_2O_3 laser

A cost effective alternative to Ti:Sapphire amplifier techniques has been demonstrated in 1993 by Ramaswamy *et.* al [78], while maintaining the advantages of the Ti:Sapphire oscillator, i.e. stability, tunability and pulse duration. The process of Cavity-dumping uses an accousto optical modulator to couple out a significant fraction of the intracavity energy (fig.6.1).

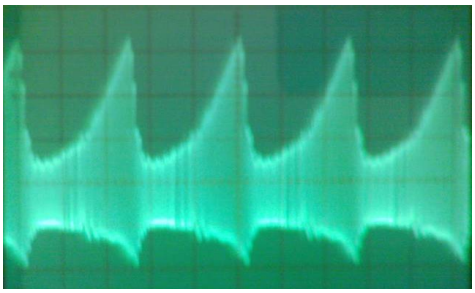

Figure 6.1: Pulse train displayed with an analog oscilloscope showing the cavity dumped operation.

The dumper (AOM) placed at Brewster's angle is electronically synchronized to the intracavity pulse train providing variable repetition rates depending on the AOM's driving electronics. The dumping process does not induce any pulse broadening or spectral filtering, thus, making it interesting for a wide range of applications.

A commercially available cavity dumped Ti:Al_2O_3 laser (*KMLabs Cascade* ™, [79]) is the seed source for the OPCPA system presented in this work. It provides up to 30 nJ of pulse energy with bandwidths of 50 nm or even more running at repetition rates of 40 kHz, 80 kHz, 200 kHz, 400 kHz, 800 kHz or 2 MHz. With an external fused silica prism compressor (see fig. 6.30) the direct oscillator output (fig. 6.2) can be compressed down to 19 fs (fig. 6.3).

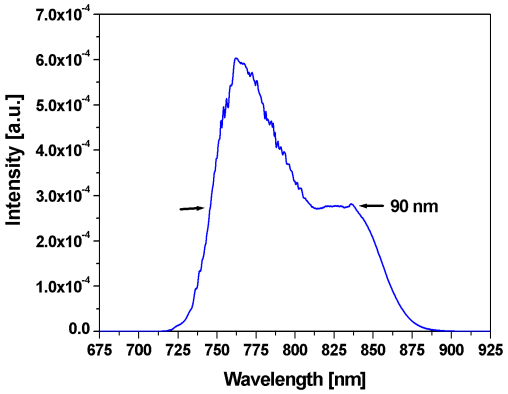

Figure 6.2: Spectrum of the cavity dumped output of the Ti:Sapphire oscillator owing a bandwidth of 90 nm.

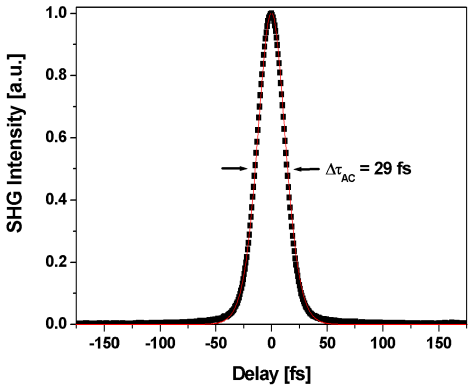

Figure 6.3: Autocorrelation trace of the pulse compressed to 19 fs (black squares) obtained with the spectrum in figure 6.2 and the AC of a corresponding $sech^2$ pulse (red).

6.3 Generation of a seed signal in the Ytterbium amplification bandwidth

In section 3.1 photonic crystal fibers are introduced as useful tool to exploit nonlinear effects, since the dispersion is tailorable. For this particular experiment the highly nonlinear photonic crystal fiber NL-3.7-975 (*Crystal Fibre*) is used. It has a core diameter of 3.7 μm, a mode field diameter of 2.9 μm and a zero dispersion wavelength of 975 nm (fig.6.4). Due to its strong confinement this fiber is suitable to frequency shift the spectrum via nonlinear dynamics. Figure 6.5 shows the spectra, that are experimentally obtained, when the fiber is seeded with a fixed spectrum (dotted blue line) and a pulse energy of

1.1 nJ (solid red line) or 8 nJ (dotted black line). The red curve shows a spectrally separated part that is within the amplification bandwidth of Ytterbium. For the purpose of this experiment it is important to investigate, if a separated compressible pulse is generated. To validate this, numerical simulations based on a split-step fourier method (fiberdesk, [80]) have been performed and experimentally a simple amplification stage has been set up with subsequent compression (fig. 6.7).

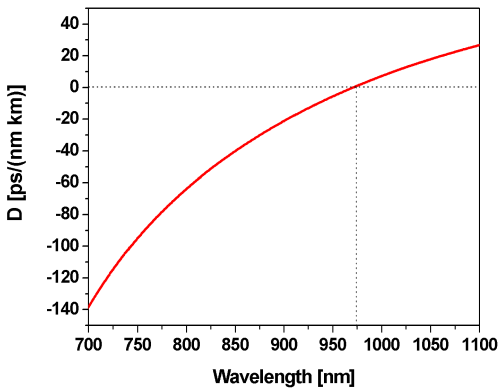

Figure 6.4: Dispersion parameter D for the PCF NL-3.7-975 with a zero dispersion at 975 nm. The parameters are extracted from fiberdesk [80].

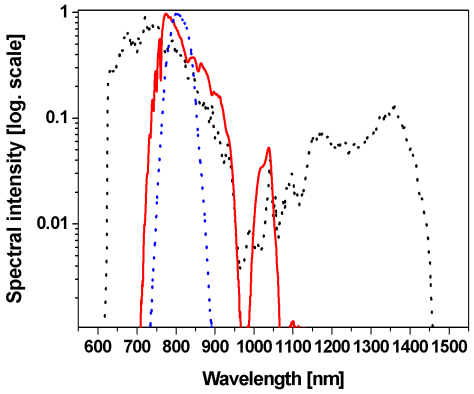

Figure 6.5: PCF NL-3.7-975 seeded with a cavity dumped Ti:Sapphire oscillator (dotted blue line). The black curve shows the spectrum for launching 8 nJ pulses that does not have spectrally isolated features while the red curve does.

The numerical simulations give an insight into the process of the pulse generation and can be understood as follows:
Since the Ti:Sapphire oscillator is running at center wavelengths of 800 nm - 850 nm, the pulses are launched to the fiber in the normal dispersion regime. The parameter N (eq. 4.13) can also be used as general propagation parameter and is referred to as soliton order in case of pumping in the anomalous dispersion regime. The typical values for the Ti:Sapphire pulses are $N \geq 6$. In the normal dispersion regime SPM dominates over dispersion for $N \gg 1$. So the spectrum of the pulse is broadened very fast, since SPM generates new frequency components that are red shifted on the leading edges and blue shifted on the trailing edges. The additional effects of normal dispersion (red travels faster than blue) lead to enhanced broadening compared with that expected from GVD alone. However, due to the large amount of SPM-induced frequency chirp the effects of dispersion

are significant and lead to a phenomenon called optical wave breaking. The generated red components travel faster than the unshifted components and pass them leading to interference at the edges of the pulse. The opposite happens with the blue components. As a results sidelobes and a fine structure near the edges (temporal domain) appear. This effect is particularly present at the initial propagation and can be clearly seen in the simulation. At a particular point the broadening process will start to be antisymmetric. This is due to stimulated Raman scattering that shifts the spectrum toward longer wavelengths. Finally, some photons in the anomalous dispersion region will be generated. The amount of photons will grow with ongoing SPM and Raman scattering. The spectral components, that are now available in the anomalous dispersion region, are separated spectrally and slow down during their propagation, so that they are also separated temporally (fig. 6.6). During their propagation they will gain energy from SPM and Raman scattering, while the latter one is also shifting the peak wavelength. Finally, the gain of energy will stop as soon as the peak power of the input pulse is too low for nonlinear dynamics.

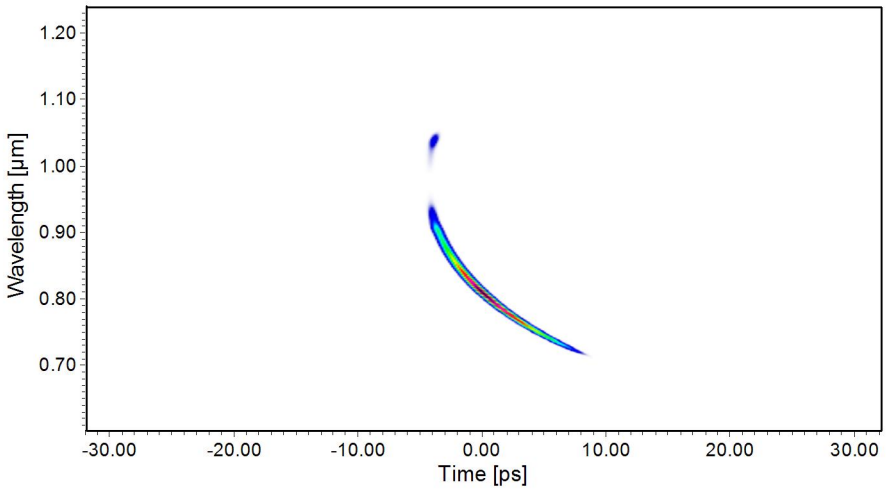

Figure 6.6: Spectrogram yielded by a numerical simulation. A sech-pulse centered at 810 nm with 1.1 nJ energy propagates through 1 m of the PCF NL-3.7-975 (see also fig. 6.9).

The center wavelength of this pulse can be fine tuned either by adjusting the length of the fiber or the input power. From an experimentalists point of view this provides a very convenient way to generate a pump pulse in the Ytterbium wavelength.

Since the generated pulse is located in the anomalous dispersion regime, it is obvious to think about the generation of a soliton (section 4.2). However, further numerical simulation revealed that this pulse broadens (temporally) during propagation and, thus, can not be considered as fundamental soliton.
A first proof-of-principle experiment (fig. 6.7) is to simply couple the cavity dumped Ti:Sapphire output to the nonlinear fiber and investigate the pulse dynamics. More than 50% of the input power can be coupled into the fiber with an aspheric lens (f=4 mm, Thorlabs, C230 TM-B). After carefully optimizing the coupling there are two parameters left to affect the nonlinear dynamics in the fiber, i.e. the input power and spectrum.

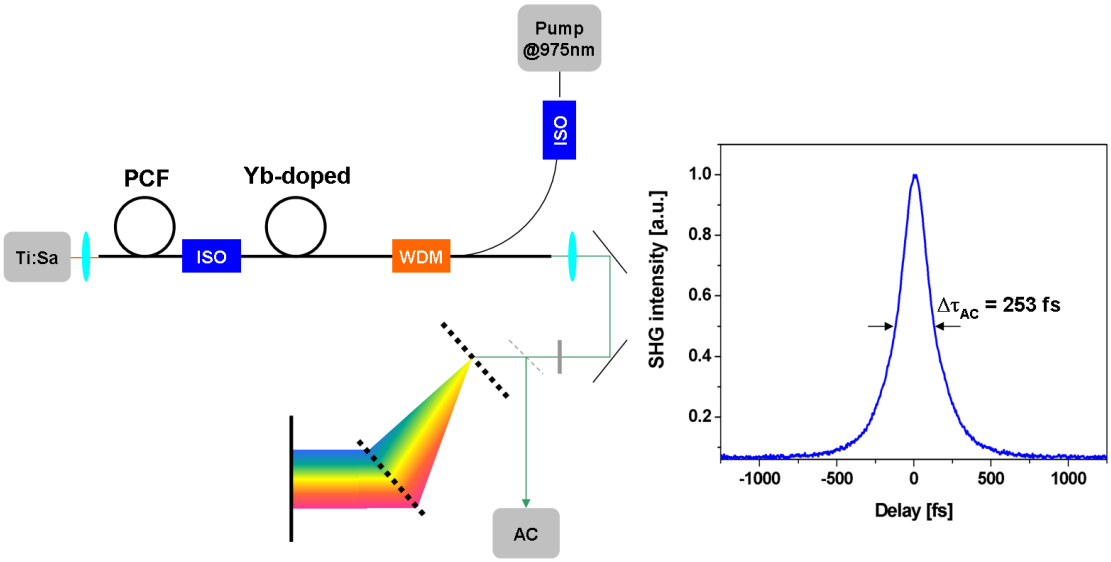

Figure 6.7: Experimental setup for the investigation of the generation of an isolated pulse. On the right side the autocorrelation trace of the amplified and compressed output is shown.

The numerical simulation predicts the generation of a pulse within the amplification bandwidth of Ytterbium and indeed it is possible experimentally, too. With this setup a pulse is generated, amplified and compressed down to 172 fs pulse duration (253 fs autocorrelation width).
Finally, experimental and numerical results are compared in figures 6.8 and 6.9, which show the dynamics of the pulse generation. A good agreement can be observed for the output spectra (fig. 6.8). In figure 6.9 the spectral evolution during propagation is shown. First the spectrum is SPM broadened and Raman shifted until overlap with the anomalous

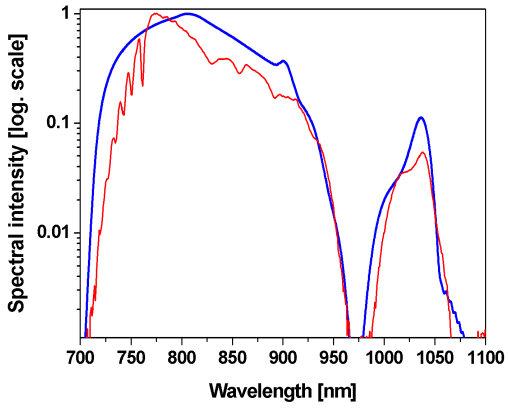

Figure 6.8: Measured output spectrum (red) of 1.1 nJ pulses coupled into 1 m PCF NL-3.7-975 and corresponding numerical simulation (blue).

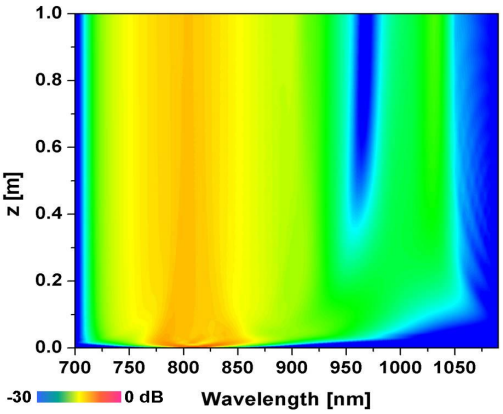

Figure 6.9: Numerical simulation: Spectral evolution of a 1.1 nJ pulse during propagation in 1 m PCF NL-3.7-975.

dispersion region is obtained that eventually leads to the generation of a isolated pulse (see preceding discussion). An estimation of the pulse energy within the amplification bandwidth of Ytterbium (centered at 1030 nm) can be performed numerically and yields a pulse energy of a few picojoule (the exact value depends on the input parameters), which is sufficient for subsequent amplification.

Further numerical and experimental investigations have shown that the pulse energy necessary to generate the pulse for the fiber amplifier depends on the center wavelength of the input spectrum. Naturally, less energy is needed when λ_0 is closer to the zero dispersion wavelength, since the spectrum does not need to be spectrally broadened so much by SPM and there is less GVD that leads to less temporal broadening resulting in a higher peak power. Measurements have shown that for a center wavelength of 845 nm only 0.6 nJ of pulse energy are needed.

To illustrate this, experimental and numerical results with the input spectra from figure 6.10 and 6.11 are presented.

Experimentally it is observed that a more stable amplification of the pulse can be obtained for a cut spectrum (fig. 6.11), particularly for center wavelengths of 840 nm or higher. The necessary input pulse energy to create a signal centered at 1030 nm does not change, since the peak is at the same wavelength both for cut and uncut spectrum. Consequently, it can be concluded that the nonlinear dynamic is basically the same for both spectra, which is

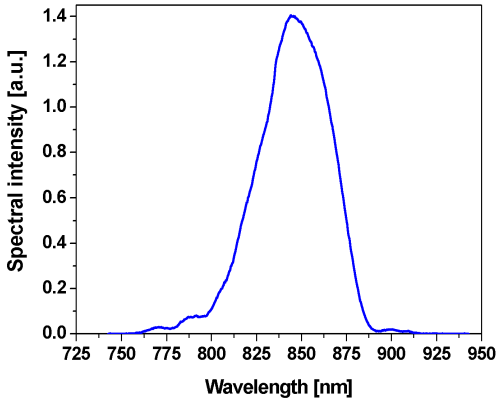

Figure 6.10: Measured spectrum before cutting it with a spectral filter.

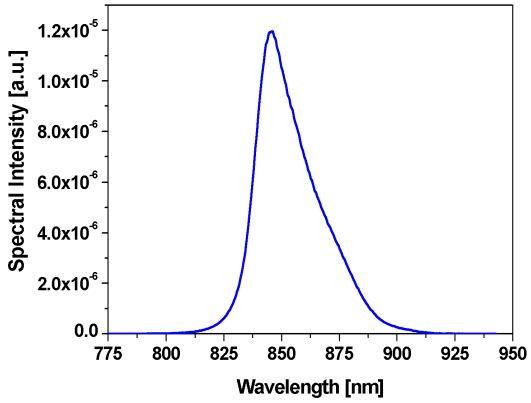

Figure 6.11: Spectrum from fig. 6.10 after cutting it with a spectral filter.

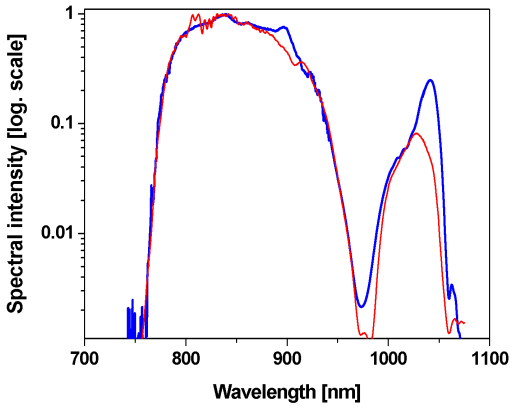

Figure 6.12: Measured output spectrum (red) of 0.6 nJ pulses with a cut spectrum (fig. 6.11) coupled into 1 m PCF NL-3.7-975 and corresponding simulation (blue).

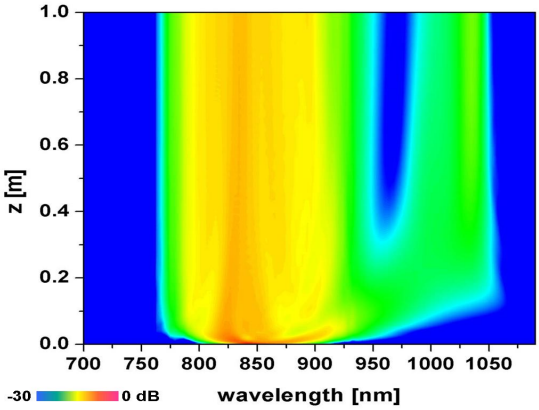

Figure 6.13: Numerical simulation: Spectral evolution of 0.6 nJ pulses during propagation in 1 m PCF NL-3.7-975 with the spectrum in fig. 6.11 and 0.6 nJ of pulse energy.

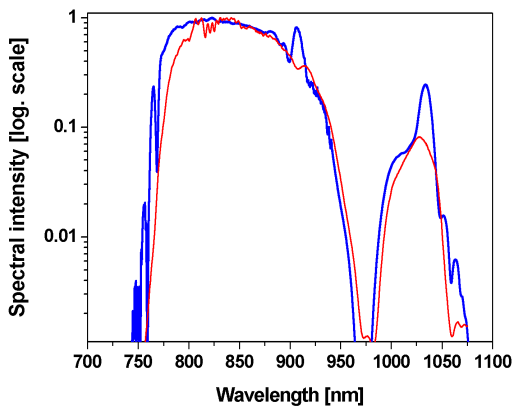

Figure 6.14: Measured output spectrum (red) after 0.6 nJ pulses with a cut spectrum (fig. 6.11) propagated through 1 m PCF NL-3.7-975. Simulation (blue) with the uncut spectrum (fig. 6.10) as seed.

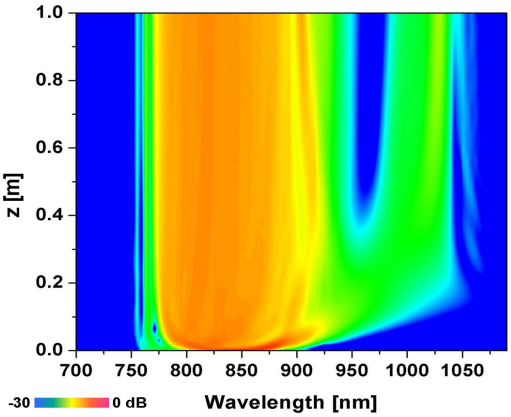

Figure 6.15: Numerical simulation: Spectral evolution of 0.6 nJ pulses with uncut spectrum (fig. 6.10) during propagation in 1 m PCF NL-3.7-975.

validated by the numerical simulations in figures 6.13 - 6.15.
So far numerical simulations could not reveal the reason for the more stable operation with the cut spectrum. A lot of parameters, e.g. input pulse energy, spectral shape, peak power, dispersion, polarization or energy fluctuations affect the propagation in the fiber. Further investigations are subject of future work.

6.4 Fiber CPA system for NOPA pump pulse generation

After creating an isolated pulse at 1030 nm (see preceding section) a monolithic fiber pre-amplifier generates enough signal for a chirped pulse fiber amplifier. A detailed experimental setup of this device is shown in figure 6.16.
The PCF NL-3.7-975 is directly spliced to a passive polarization maintaining (PM) fiber. For alignment purposes this piece of fiber contains a FC plug with angle polished end facets to suppress lasing. It can directly be coupled into a spectrometer in order to monitor the pulse generation. The other end of the PM fiber is spliced to the pre-amplifier that consists of several stages (fig. 6.16). A fiber optical circulator is used to build a double pass amplifier. The reason for setting up this device is to saturate the amplifier and, hence, effectively suppress ASE. Signals entering this device at port 1 propagate through 30 cm

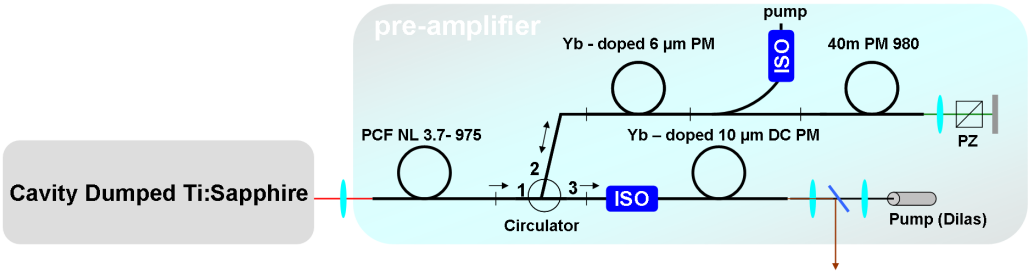

Figure 6.16: Setup of the pre-amplifier. PZ - polarizer

of Ytterbium-doped 6 μm core fiber (port 2), that is pumped by a fiber coupled Bookham Diode running at 300 mW CW-power and a center wavelength of 975 nm. The pump source is coupled to the active fiber via a wavelength division multiplexer (WDM). 40 m of passive polarization maintaining fiber are added in order to ensure the temporal overlap in the NOPA-stage and to stretch the pulses for the purpose of reduced nonlinearity in the pre-amplifier.

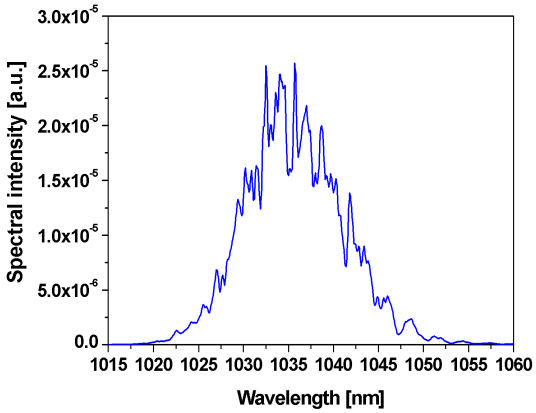

Figure 6.17: Spectrum after the pre-amplifier.

The signal is reflected on a mirror after passing a polarizer (PZ), that is used to suppress ASE, and recoupled after passing the polarizer (PZ) again. Finally, the signal is amplified for the second time and leaves the circulator at port 3 with approximately 1 nJ of pulse energy and a pulse duration of 80 ps. 2.2 m of Ytterbium-doped double clad fiber is used

to boost the average power up to 1.2 W. The fiber has a 125 μm pump core, a 10 μm active core and is pumped with a fiber coupled DILAS laser diode (200 μm core, NA=0.2) that is emitting at 975 nm. To keep the nonlinearity low, the pre-amplifier runs in such a way that the average output power is 360 mW corresponding to a B-Integral of B=2.6 (eq. 6.1). The output spectrum after the pre-amplifier is shown in figure 6.17.

6.4.1 Chirped pulse fiber amplifier

For efficient conversion, both in the SHG and the parametric amplification, the peak power of the pulses needs to be high enough and the temporal shape needs to be clean and without pre-pulses.
A main limitation for fiber based amplifier systems are pulse distortions due to nonlinear effects [21]. A severe issue is the phase imposed by SPM that can lead to a nonlinear chirp, which can not be compensated by common compressor setups since they introduce, or remove, a linear chirp. To quantify the effects of SPM a parameter B, the B-integral, is introduced. It is found to be [81]

$$B = \frac{2\pi}{\lambda} \cdot \int_0^L n_2 \cdot I(z) \cdot dz, \tag{6.1}$$

where $I(z)$ is the pulse intensity varying over the fiber length L. For B$\leq$1 the propagation is considered as linear, while for higher values of B, SPM leads to pulse broadening and the formation of sidelobes that can contain a significant amount of energy.

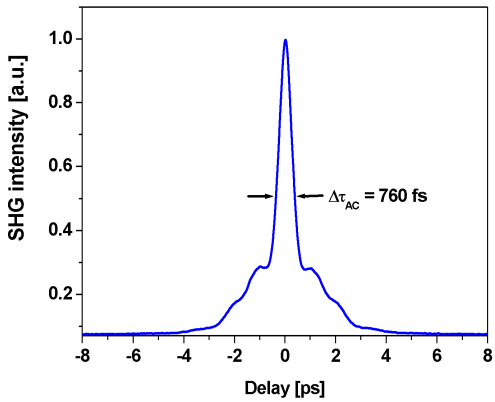

Figure 6.18: Autocorrelation at 400 kHz, 16 μJ and a B-Integral >25.

To avoid nonlinear distortions a fiber based CPA system is used for the presented experiment consisting of the parts described in figure 4.1. To stretch the pulses, either a fiber stretcher or a bulk grating stretcher can be used. A first test revealed, that stretching the pulse in approximately 100 m passive fiber leads to wings in the amplified and compressed pulse (fig. 6.18) that cause very poor conversion efficiencies (<10%) in the SHG process, so that the NOPA stage can not be operated. The autocorrelation trace shows a pedestal, that is due to nonlinear phase offset and third order dispersion. The main amplifier is operated at a B-Integral of B > 25 (400 kHz,10.5 W output power), which indicates a huge nonlinear distortion that can not be compensated. Therefore a grating stretcher is set up as shown in figure 6.19 in order to increase the stretching factor and, hence, reduce the B-Integral.

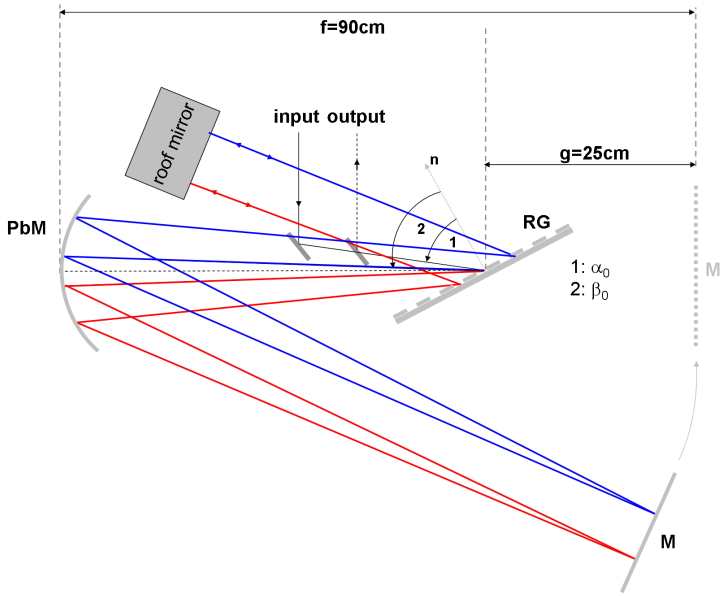

Figure 6.19: Setup of the grating stretcher. In the experiment the plane silver mirror (M) is at the position of the dotted line and is moved in this sketch for a better illustration. PbM - parabolic mirror, RG - reflection grating (gold, 1740 g/mm), M - plane silver mirror, n - grating normal

The basic idea of a stretcher is to slightly displace the grating (RG) from the focal point of the imaging optic, a parabolic mirror (PbM) used to reduce chromatic aberrations that arise from focusing with lenses. If the grating is placed at the focal point, i.e. where the plane silver mirror (M) is positioned, all spectral components travel the same optical

path length. By moving the grating inside the focal length stretching is achieved. For a displacement g the second derivative of the phase $\Phi(\omega)$ with respect to the frequency reads as

$$\Phi^2(\omega) = \frac{d^2\Phi(\omega)}{d\omega^2} = -2 \cdot g \cdot \frac{m^2\lambda_0^3}{\pi c^2 \Lambda^2 \cos(\beta_0)}, \tag{6.2}$$

where m is the order of diffraction, c the speed of light, λ_0 the center wavelength of the pulse, Λ the grating period and β_0 the diffraction angle of the center wavelength. In this setup the input beam is reflected by a mirror onto the gold coated reflection grating with 1740 grooves per mm, which is equal to a grating period of $\Lambda = 0.57\,\mu$m. Depending on the angle of incidence α_0 and the wavelength λ the spectral components are diffracted in an angle β determined by [82]

$$\beta = \arcsin\left(\frac{m \cdot \lambda}{\Lambda} - \sin(\alpha_0)\right). \tag{6.3}$$

The parabolic mirror slightly focuses the spectrum onto the plane silver mirror that reflects it back to PbM and from there on the grating. Now it is parallel to the input beam, but the spectral components are spatially separated, what is referred to as spatial chirp. To remove the spatial chirp the spectrum has to pass the same setup vice versa. The size of the stretcher can be reduced by using a roof mirror. It reverses the beam while it also changes its height. So the reflected beam is down steered without any spherical aberrations that would arise from a plane mirror that is slightly misaligned. After passing the setup again all spectral components are located in one beam and leave the stretcher slightly lower than the input beam. In order to obtain a good temporal pulse quality, it turned out to be useful to cut the spectrum in the stretcher setup. For this purpose two beam blocks are put in front of the plane silver mirror that are slowly shifted inwards until the autocorrelation of the amplified and compressed pulse is sufficient.
The spectrum is cut to about 6 nm (fig. 6.20) and the pulse duration is measured with a fast photodiode and a sampling oscilloscope to be 320 ps $\pm$ 20 ps (fig. 6.21). A simple calculation of the second order dispersion can be performed with the help of equation 6.2. For m = 1, $\lambda_0 = 1036$ nm, $\Lambda = 0.57\,\mu$m, g = 25 cm and $\beta_0 = (69.5 \pm 0.5)^\circ$ the dispersion is $\Phi^2(\omega)$ = -39.7 ps/nm. The 80 ps input pulse with a bandwidth of 6 nm is therefore additionally stretched resulting in a pulse duration of 318 ps $\pm$ 34 ps. This agrees very well with the experimental results.
Due to the large stretching the spectral and temporal shape are equal. Hence, the spectral cutting results in a nearly rectangular temporal pulse profile (fig. 6.21). So the effective peak power is lower at the same energy compared to a gaussian shape, and therefore, nonlinear distortions are reduced [83]. This explains why the temporal pulse quality of the

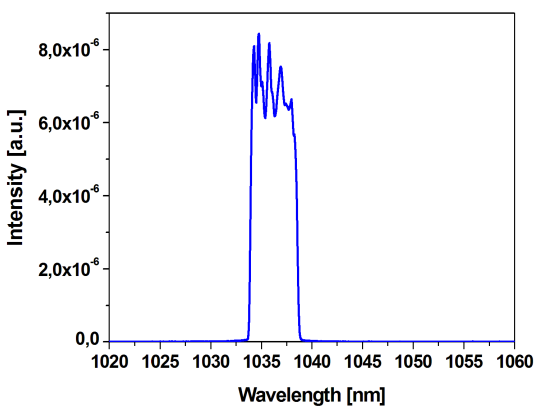

Figure 6.20: Cut spectrum after the stretcher. The FWHM is estimated to be 6 nm.

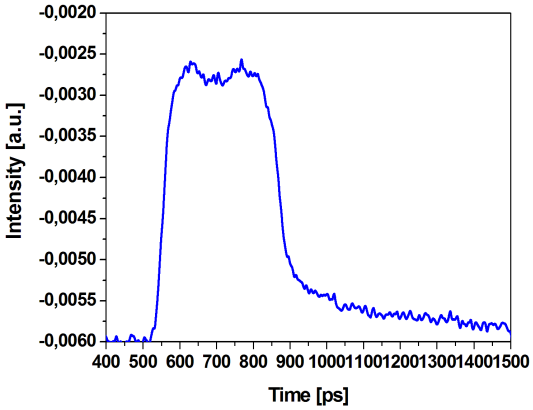

Figure 6.21: Stretched pulse. The FWHM duration, measured with a fast photodiode and a sampling oscilloscope, is 320 ps.

amplified and compressed pulses is better with spectral cutting.
Of course, cutting the spectrum results in a very poor throughput of the stretcher. More than half of the power is lost due to the cutting process and almost another factor of two due to the mirrors (especially the poor quality of the silver mirror and the diffraction efficiency of the gold gratings affects the throughput). Finally, an average power throughput of 170 mW (50 mW) was measured for an output of the pre-amplifier of 1.2 W (360 mW). The main amplifier is a 1.7 m long polarizing double clad Ytterbium-doped photonic crystal fiber (DC - 200/40 - PZ - Yb - 01, *Crystal Fibre*). It has a signal core diameter of 40 μm, a mode field diameter (MFD) of 29 μm $\pm$ 2 μm and an inner cladding diameter of 200 μm with a NA of 0.55$\pm$0.05 [84].

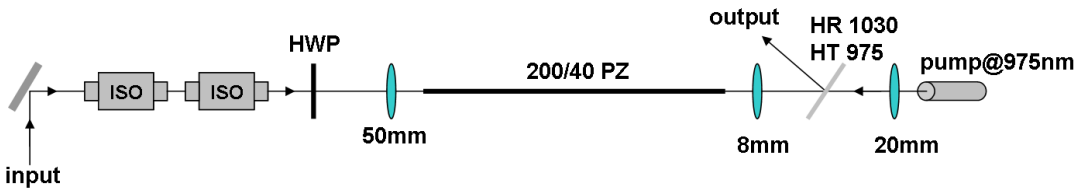

Figure 6.22: Setup of the main amplifier.

Figure 6.22 shows the setup for the main amplifier. The beam emerging from the stretcher passes two isolators that suppress lasing, but also decrease the power a bit, so that approximately 60 mW of seed power are available for 170 mW compressor output. The power is lost at the isolators due to ASE underground and wrong polarization.
The amplifier fiber is pumped by a CW multimode laser diode emitting at 975 nm in the opposite direction. The amplified signal is sent to the compressor via a dichroic mirror that is highly reflective for 1030 nm, but highly transmissive for the pump radiation.

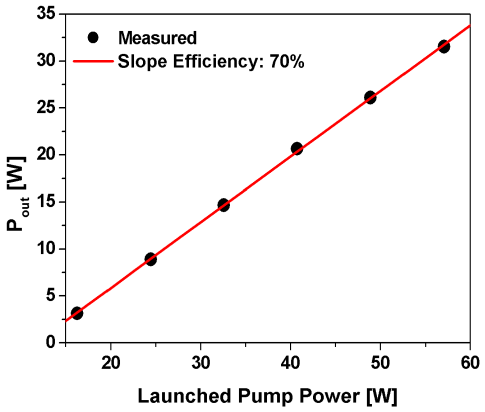

Figure 6.23: Output power of the main amplifier with respect to the pump power for 60 mW seed.

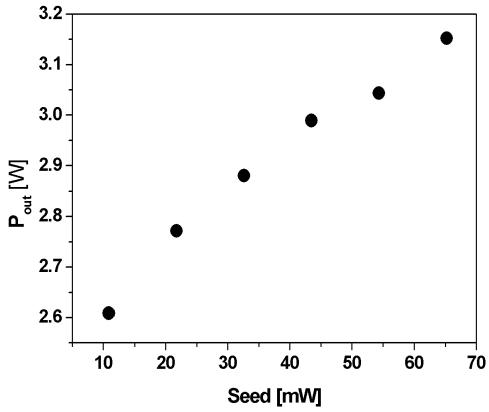

Figure 6.24: Output power of the main amplifier with respect to the see power for a pump power of 15 W.

A slope efficiency of 70% and average output powers well above 30 W at 2 MHz repetition rate are obtained (fig. 6.23). The efficiency of pump light coupling is measured[1] to be 75% so that the launched pump power can be calculated. For a launched pump power of 58 W the average output power is 31 W resulting in a pulse energy of 15.5 μJ. The B-Integral for this amplifier is calculated to be 3.4 (for 60 mW of seed power) and, hence, some distortions due to nonlinear phase offset can be expected after compression. Figure 6.24 shows the output power with respect to the seed power for a fixed pump power of 15 W. A small seed saturation effect can be observed, but full saturation is not achieved so far.
To dechirp the pulses a simple grating compressor consisting of two gold coated gratings with 1740 grooves/mm is used (fig. 6.25). In order to compensate even the third order dispersion that is imposed by the long fiber lengths in the pre-amplifier the diffraction

[1] A short piece of fiber ($\approx$ 2 cm) is used to neglect absorption. Input and output power are measured, while a pinhole is used at the output side to measure only the light in the pump core.

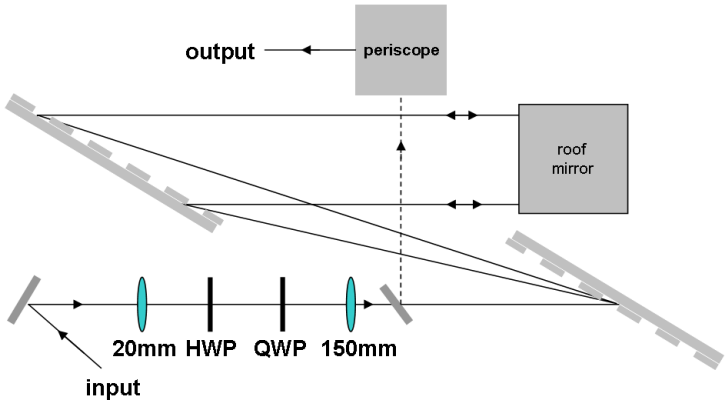

Figure 6.25: Setup of the grating compressor.

angle is slightly increased compared to the stretcher. Thermal damage is avoided by increasing the beam diameter to 20 mm by a telescope (fig. 6.25). The efficiency of the compressor is measured to be more than 65% resulting in a compressed pulse energy of 10 μJ (20 W average power). After optimizing the grating distance and the diffraction angles pulse durations below 1 ps are easily obtained as can be seen in figure 6.26.
For a compressed pulse energy of 0.6 μJ (B=0.4) a very clean pulse shape is obtained while for 10 μJ of compressed output energy wings become apparent. The autocorrelation width of the high energy output is measured to be 1.2 ps. Fourier transforming the output spectrum of the main amplifier (fig. 6.27) and subsequent addition of dispersion leads to a deconvolution factor of 1.64 and, therefore, a pulse duration of approximately 730 fs. Note that the real pulse duration might differ a little bit from this value. A simulation yields a peak power of 10 MW with approximately 20% pulse energy in the wings, caused by nonlinear phase distortions due to the value of B=3.4.
Finally, to generate the pump signal, the compressed output has to be frequency doubled in a nonlinear crystal. The process of SHG has already been investigated in section 5.2. For Type I phase matching purposes the crystal is cut in the right angle to the optical axis. It is fixed in a rotatable mount in order to optimize the SHG signal. Different crystals, e.g. BBO, KDP and LBO, have been used with varying lengths. Most efficiently for frequency doubling turns out to be a 2 mm LBO (Lithium Triborate) crystal cut with $\theta = 13.8°$, an anti reflection coating and a damage threshold >10 GW/cm^2 for 10 ns pulses [85]. The compressed infrared beam is focused to 80 μm spot size in the crystal resulting in an

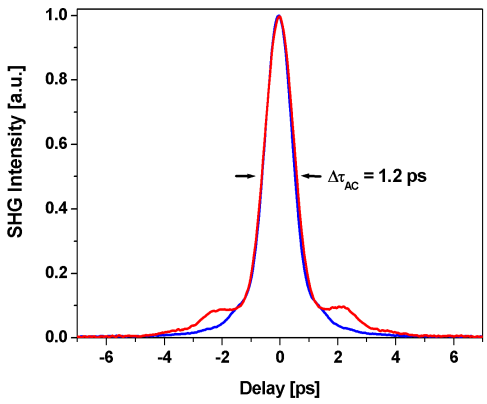

Figure 6.26: Autocorrelation trace for a compressed pulse energy of 0.6 μJ (blue) and 20 μJ (red).

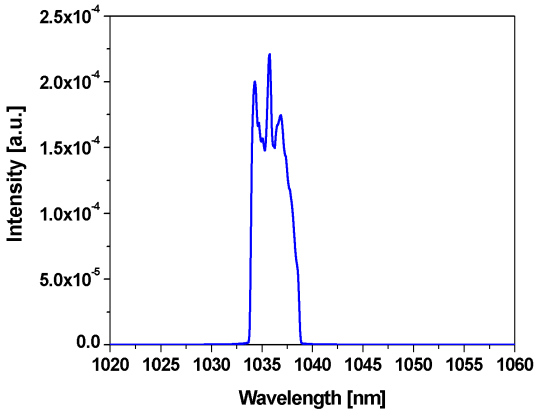

Figure 6.27: Output spectrum of the main amplifier.

intensity as high as 50 GW/cm^2 whereas no crystal damage occurs.
The spectrum (fig. 6.29) of the second harmonic generation has a FWHM bandwidth of 1 nm. In 6.28 the second harmonic power and the conversion efficiency are shown with respect to the compressed output power. Interestingly the highest conversion efficiency of 49% belongs to a compressed output power of 9 W (4.5 μJ). For this experimental parameters the B-Integral of the main amplifier is 1.2, so that only a small amount of energy is located in the wings of the pulse. With increasing output power more and more energy is shifted to the wings and can not be frequency doubled, therefore, reducing the conversion efficiency. The decreasing conversion efficiencies for output powers smaller than 9 W are due to the lower intensities that do not allow for efficient nonlinear processes.
A maximum pump power of 8.3 W can be obtained for the NOPA stage with a compressed output power of 20 W. An estimation of the pulse duration for the SHG beam can be performed with the split-step integration method based freeware SNLO [86] and yields 620 fs resulting in a peak power of 6.7 MW. Parametric amplification in the NOPA stage requires intensities of the order of 20 GW/cm^2 that can be reached by focusing to diameters of 100 μm or smaller.

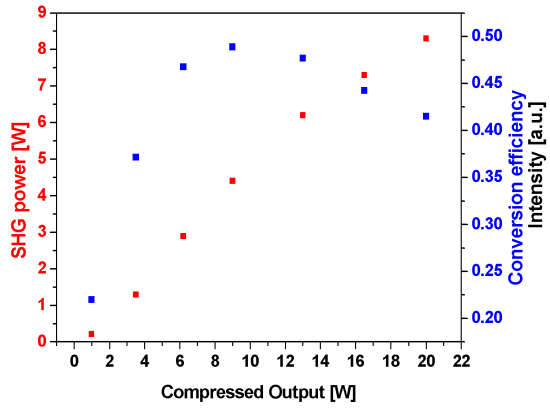

Figure 6.28: Obtained SHG power (red) and corresponding conversion efficiencies with respect to the compressed output power.

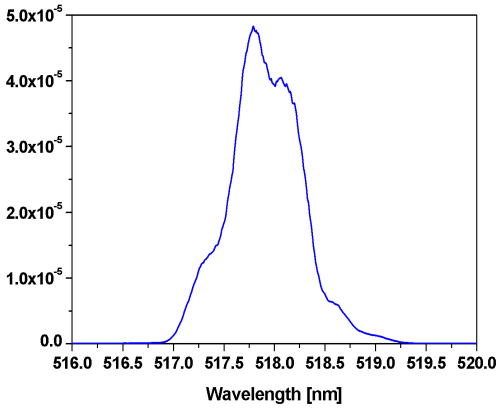

Figure 6.29: Spectrum of the second harmonic signal.

6.5 Non-collinear optical parametric amplification

In section 5.3.2 advanced parametric amplification designs are discussed. It is well known that these devices can offer a large amplification bandwidth [68], [87] that is required for the generation and amplification of ultrashort light pulses. Particularly favorable for the amplification of Ti:Sapphire pulses is BBO (Beta Barium Borate), that provides amplification for signal wavelengths of 700 nm to 900 nm when a non-collinear geometry is used, the pump wavelength is 518 nm and the angle of signal and pump is set to be 2.5° (fig. 5.4). According to the phase matching curve in figure 5.4, the BBO crystal used for this experiment is cut at an angle of 22°.
With enough peak power available in the pump beam the low energy Ti:Sapphire pulse can be amplified in the BBO crystal. If spatial and temporal overlap is achieved, sufficient amplification is expected.

6.5.1 Direct amplification of Ti:Sapphire pulses

Figure 6.30 shows the setup for the amplification stage that is used for both experiments presented in the following sections.
The temporal overlap of signal and pump can be fine tuned with a delay stage, while a good approximation can be obtained with a fast photodiode. For this purpose the diode is

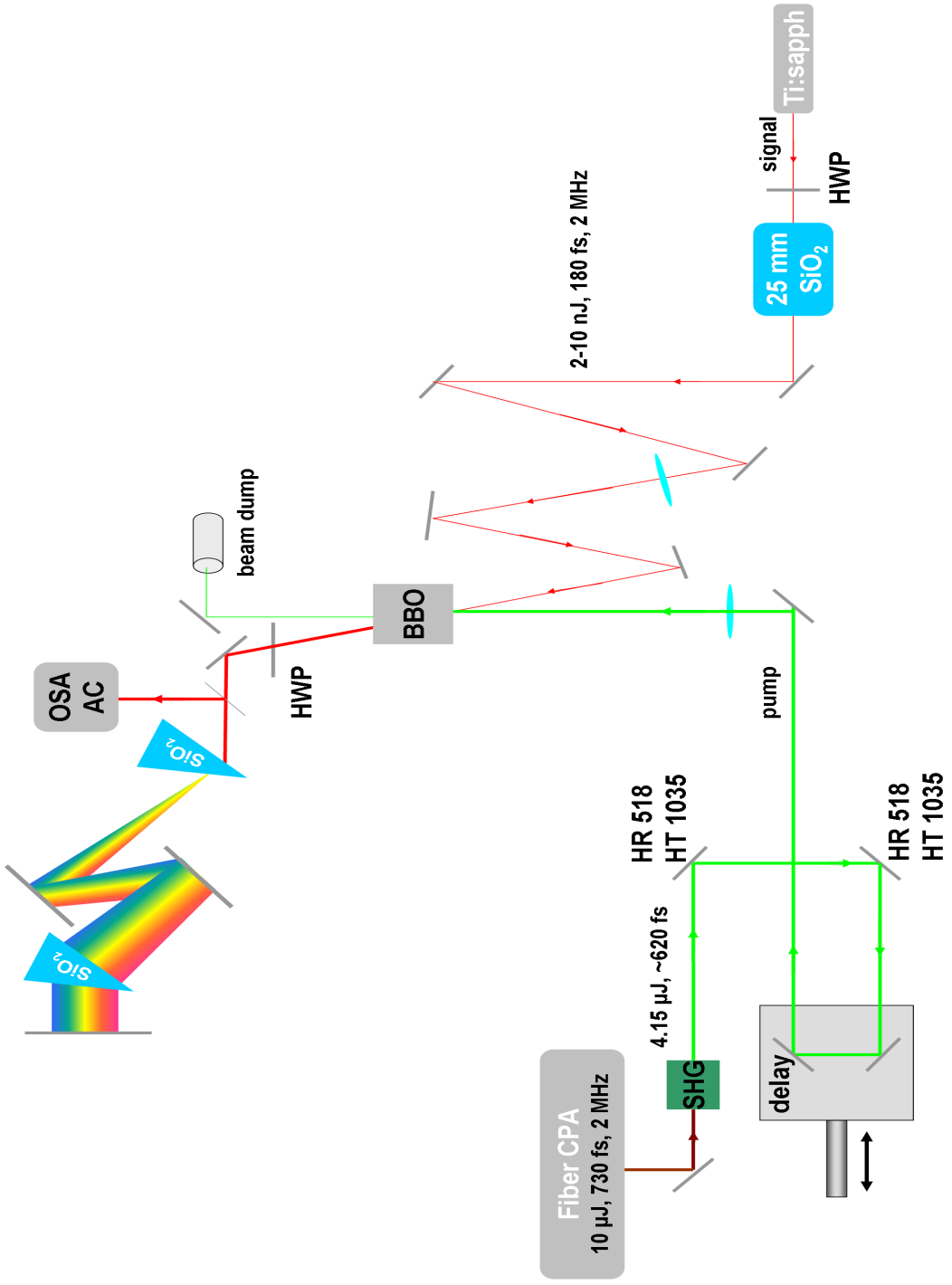

Figure 6.30: Setup of the NOPA setup with subsequent fold prism compressor.

put at the spatial overlap point (after the crystal is removed). The next step is to watch the signal and pump pulses at the oscilloscope and determine their temporal distance. With the help of this fast photodiode the (temporal) mismatch can be specified to an accuracy of a few 100 ps (≈ 3 cm-12 cm). To compensate the mismatch, a certain length of fiber at the end of the double pass preamplifier (fig. 6.16) can be added or removed in a very convenient way. This also offers the possibility to change the repetition rate without changing much of the setup.
For OPCPA systems the signal pulse duration with respect to the pump pulse duration is important [88]. Understandably, for a short signal pulse (<1/4 of the pump pulse duration) the whole bandwidth is amplified, but energy can not be extracted efficiently from the pump pulse, while for a long signal pulse (>1/2 of the pump pulse duration) only a part of the signal spectrum is amplified due to low intensities in the wings of the pump. Finally, it has to be traded off between conversion efficiency and amplification bandwidth (fig. 6.31).

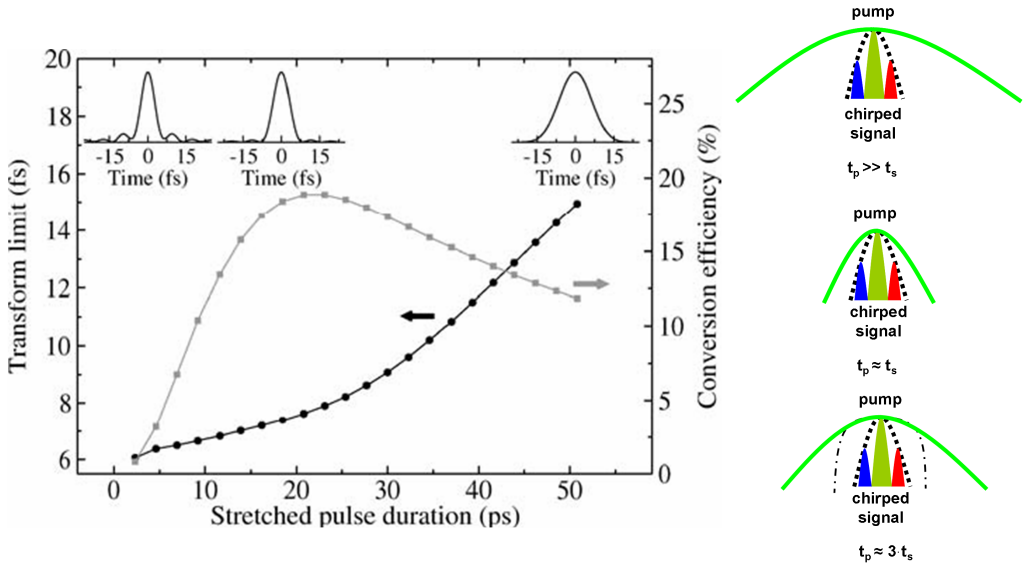

Figure 6.31: Simulation showing the conversion efficiency and transform limit of seed pulses with different durations for 60 ps Gaussian pump pulses (figure from [88]). The right side shows a schematic illustration of the seed to pump ratio. The optimum is found to be $\tau_s \approx 0.2 - 0.3 \cdot \tau_p$.

In [88] numerical simulations have been performed to yield the optimum seed pulse duration for a given pump pulse duration. For Gaussian pump pulses the signal duration should be about 0.2 - 0.3 times the pump pulse duration. More efficient conversion would be ob-

tained for a top hat pump pulse profile as depicted in figure 6.31 (bottom right side). In the presented NOPA setup the SHG signal is estimated to have a duration of 620 fs resulting in a required seed pulse duration of 124 fs-186 fs. Experimentally different stretching factors have been investigated, which can be seen in table 6.1. They validate the results of the numerical simulation, since a good conversion efficiency has been obtained for a seed duration of 0.3 times the pump pulse duration. Finally, 25 mm of fused silica are used to run the experiment resulting in a pulse duration of about 186 fs.

Amount of glass	τ_{seed} [fs]	τ_{seed}/τ_{pump}	P_{out}
3 mm	70	0.11	600 mW
50 mm	324	0.45	400 mW
25 mm	186	0.30	1000 mW

Table 6.1: Output power of the NOPA system for different seed pulse durations validating the results of [88].

To align the crystals θ angle, only the pump is applied. For high intensities, parametric fluorescence, a quantum phenomenon, can be observed. Due to zero-point vacuum fluctuations that interact with the pump, a nonlinear polarization is produced that radiates at all frequencies [64]. Of course, radiation is only present if the phase matching condition is satisfied. Advantageously, the parametric fluorescence can be used to align the crystal position.

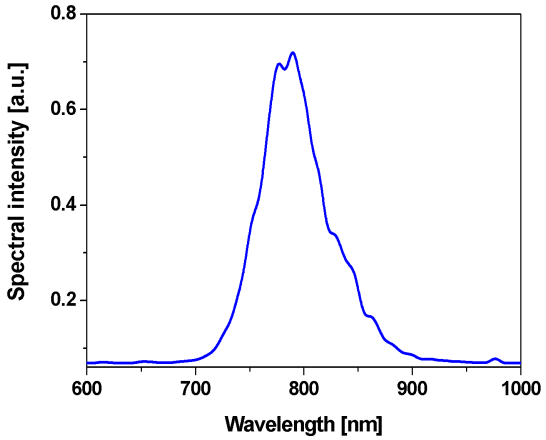

Figure 6.32: Superfluorescence spectrum of a 5 mm BBO.

Assuming to have spatial overlap in the crystal and the right pump - seed angle (α), the pump radiation is blocked while a spectrometer is put in the signal beam after the crystal. Next, the seed is blocked and the pump radiation is applied. Now the crystal can be rotated (θ) until the superfluorescence can be seen on the spectrometer (fig. 6.32), meaning that amplification is supposed to occur in the signal direction. With both seed and pump applied, only the delay needs to be fine tuned until amplification can be observed.
The amplified Ti:Sapphire pulses are finally compressed with a fused silica prism compressor and monitored with a spectrometer and/or an autocorrelator. A computation of the amount of dispersion for the signal shows that the prism distance needs to be of the order of a few meters, so that two mirrors are used to fold the compressor.
The first experiment that is performed with this setup is the direct amplification of the Ti:Sapphire oscillator output. The alignment has been done in the way described above and the geometry, the spatial and temporal overlap have been optimized for the best results.

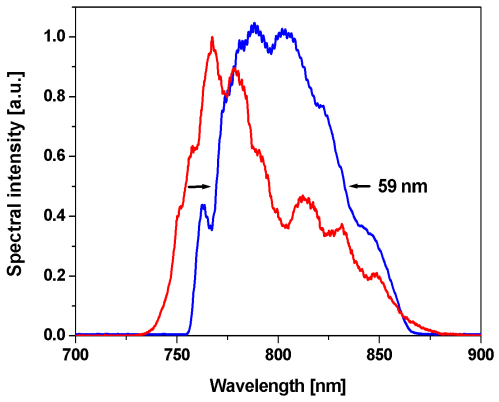

Figure 6.33: Normalized spectrum of the seed pulse (red) and amplified pulse (blue).

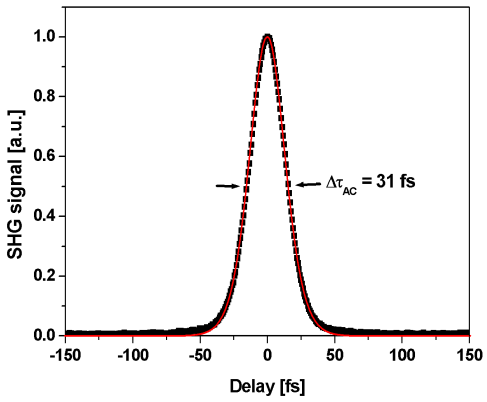

Figure 6.34: Autocorrelation trace (black squares) and a sech^2 fit (red).

The amplified bandwidth is estimated to be 59 nm (fig.6.33). Note that the spectral shape improves during amplification. Subsequent compression with the prism compressor (fig. 6.30) yields an autocorrelation width of 31 fs resulting in 20.1 fs pulse duration assuming sech^2 pulse shape (6.34). The maximum output power of 1.1 W (550 nJ) is achieved by focusing the pump beam to 80 μm diameter ($\approx$ 100 GW/cm^2). This equals a conversion efficiency of 13 %. Indeed, the beam profile is strongly elliptical, but can be improved by moving the focus slightly behind the crystal. For 1 W avergage power (500 nJ pulse

energy, 12 % conversion efficiency) a decent beam profile is measured that could be improved to the account of conversion efficiency (fig. 6.35).

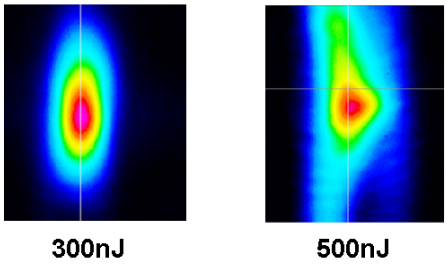

Figure 6.35: Beam profiles of the NOPA for conversion efficiencies of 7 % (300 nJ) and 12 % (500 nJ).

The overall performance is characterized, either with a varying pump power for a fixed seed or a varying seed power for a fixed pump power. Figure 6.36 shows that a gain factor of ≈55 can be achieved for this particular experiment with 15 mW of seed power. Normally, higher gain factors are expected for these intensities, but the Gaussian like spatial and temporal profiles only permit efficient conversion in the high intense parts.

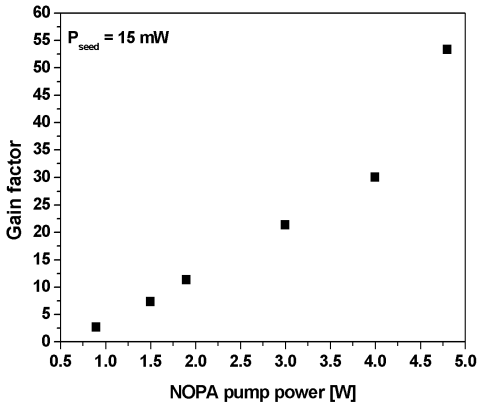

Figure 6.36: Gain with respect to the pump power for a fixed seed power of 15 mW (7.5 nJ).

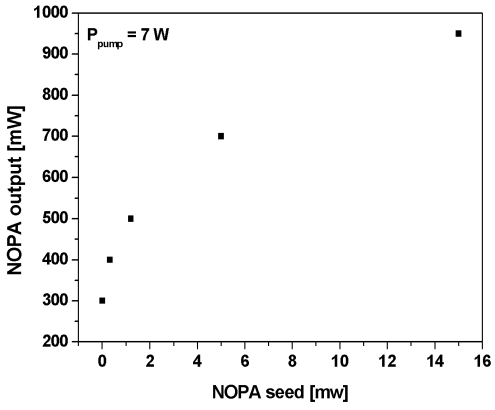

Figure 6.37: Amplified signal power with respect to the seed power for a pump power of 7 W (3.5 μJ).

The curve in figure 6.37 indicates that the NOPA's amplification tends to saturate. In this particular case one would expect the amplified spectrum to be top-hat-shaped. Indeed, the wings of the amplified spectrum in figure 6.33 rise, but do not form a plateau with the peak at all. In conclusion it is to say, that full saturation is not achieved so far, but effects of saturation can already be observed. Further investigations require numerical simulations.

6.5.2 Spectrally broadened Ti:Sapphire and generation of sub 20 fs pulses

To benefit even more from the enormous bandwidth of parametric amplification, a highly nonlinear photonic crystal fiber is used to broaden the Ti:Sapphire spectrum via self phase modulation (sect. 4.2.1). For broadening purposes the PCF NL-4.7-1030 fiber (*crystal fibre*) has been used. Its zero dispersion wavelength is at 1030 nm making it suitable for this experiment, since broadening into the anomalous dispersion regime can lead to soliton formation and break up, that adds phase terms that can not be compensated for.

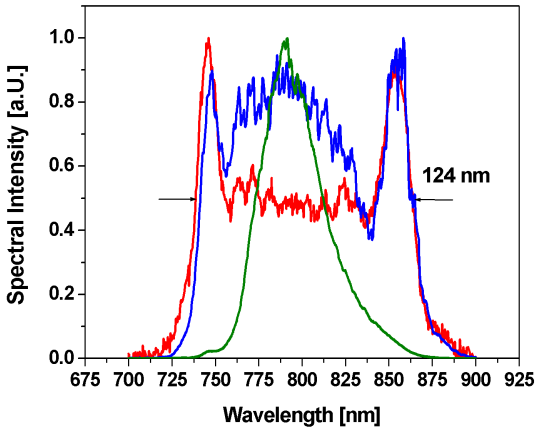

Figure 6.38: Spectrum of the Ti:Sapphire (green), the SPM spectrum (red) and the amplified spectrum (blue).

By coupling 5 nJ of pulse energy into the fiber the width of the spectrum is increased from 39 nm to 124 nm (fig. 6.38). Note that the spectral bandwidth of the Ti:Sapphire oscillator is lower, because a more stable operation is obtained for dumping 30 nJ of pulse energy. To obtain a seed pulse duration of about 180 fs, the broadened pulses need to pass a

chirped mirror pair (-35 fs^2/bounce) five times (10 bounces), before being applied to the BBO crystal. Finally, amplification lowers the "batty" structure (fig. 6.38), because the center parts of the spectrum meet the more intense center of the pump pulse.
The whole spectrum can be amplified, but the output power was just 600 mW (300 nJ) due to the fact that the average signal power was lower than in the preceding experiment.

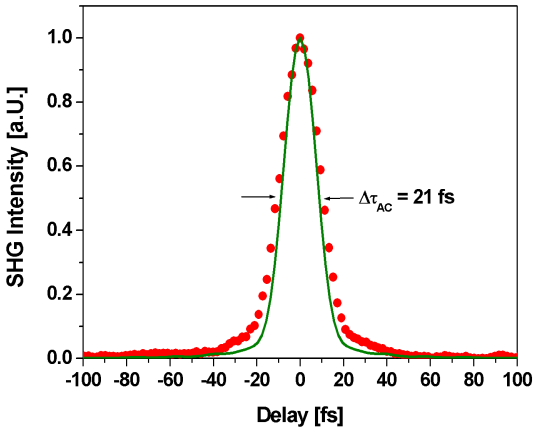

Figure 6.39: Autocorrelation of the compressed NOPA output (red squares) and transform limit (green).

Compressing the output with the prism compressor yields pulses with an autocorrelation width of 21 fs (fig. 6.39). Fourier transforming the spectrum gives a deconvolution factor of 1.35. So the pulse duration is 15.6 fs which is only slightly above the transform limit (13.2 fs). Due to spectral structure, nonlinear phase and uncompensated higher order dispersion small wings become apparent in the autocorrelation trace (fig. 6.39).

6.6 Summary

The presented experiments show a novel approach for the amplification of broadband Ti:Sapphire pulses at high repetition rates. It has been proven that a self-synchronized high average power Ytterbium-doped fiber amplifier system can be used to transfer its energy to the oscillator pulses in a nonlinear crystal. So the unique properties of a Ti:Sapphire are combined with the average power scalability of fiber based chirped pulse amplification systems. The experimental conditions for the generation of a stable fiber amplifier signal via nonlinear dynamics in a photonic crystal fiber are investigated in detail. Efficient parametric amplification is achieved by pumping the NOPA with the frequency doubled output of the fiber CPA system. Finally, amplified pulse energies of up to 500 nJ can be obtained and subsequent compression with a fused silica prism compressor produces pulses as short as 20.1 fs leading to a peak power of 20 MW.
Additional spectral broadening in a 1.5 cm PCF NL-3.7-1030 increases the bandwidth to 124 nm. Amplification of the SPM broadened spectrum leads to 300 nJ pulse energy and a compressed pulse duration of 15.6 fs. The whole setup is operated at a repetition rate of 2 MHz.

Chapter 7

Summary and outlook

A detailed investigation of the capability of fiber amplifier based optical parametric chirped pulse amplification systems (OPCPA) for the generation of high-energy ultrashort pulses is provided by this thesis. Additionally, the required pulse parameters for high-harmonic generation are investigated in order to evaluate possible applications of the OPCPA system, e.g. lensless imaging.
Limited to synchrotron facilities before, a tabletop lensless imaging experiment has been performed. Of course, it can not compete with the overall flux of these, but due to the compact size (the microscope setup has a footprint of just 1.5 m $\times$ 0.5 m without the HHG source), it is of great interest for a variety of applications concerning biology, material science or lithography. A resolution down to 214 nm has been obtained making it already competitive to state-of-the-art "conventional" microscopy techniques. The ease of alignment and handling is a great advantage compared to synchrotron sources. Future improvements will basically focus on pushing the resolution, hence, making it possible to see even smaller structures. This can be achieved by using higher order harmonics or advanced detector designs. Improved imaging technologies such as multiple reference Fourier transform holography could help to work with a low number of photons [89]. Additionally the raising speed of computers can help to make the reconstruction faster. Still, there remains a drawback that can not be overcome with todays Ti:Sapphire laser technology: The poor conversion efficiencies of high-harmonic generation combined with the low repetition rate of the driving laser system lead to long integration times and can only be overcome by up-scaling the laser average power.
The second part of this work shows an alternative to common Ti:Sapphire amplifier technology , not only to make the HHG, and hence, the lensless imaging faster, but also to enhance other processes initiated by high-intensity laser pulses and suffering from low conversion efficiencies. Increasing the repetition rate would substantially improve the ap-

plicability of these processes.
The unique properties of a Ti:Sapphire oscillator are combined with the average power, and therefore, repetition rate scalability of a fiber amplifier by the means of a non-collinear optical parametric chirped pulse amplifier. The system is operated with 2 MHz producing pulses with energies up to 500 nJ and pulse durations down to 15 fs with very clean pulse shape. As previously mentioned (section 2.4), high-harmonic generation and its application to lensless imaging requires intensities of the order of 10^{14} W/cm^2. So far the parametric amplification can provide roughly 10^{11} W/cm^2 (500 nJ, 20 fs, 100 μm spotsize). Consequently, the possible experimental improvements must be capable of increasing the intensity by a factor of 10^3.
Fortunately, there are promising approaches. For example, fiber technology, in principle, is capable of producing average power in the kW range. Latest experiments have shown a fiber CPA system operating at 1 mJ pulse energy and 100 kHz repetition rate [23]. The combination of kW average power and mJ pulse energy seems to be achievable with state-of-the-art fiber technology. Furthermore, advanced experimental designs can help to tune up the performance of the system. If intense nanosecond pump pulses would be available, the seed pulse could be stretched to longer pulse durations than in the presented experiment making the energy transfer more efficient. Another possibility to power scale the output is an amplifier chain, i.e. several nonlinear amplifier crystals. Detailed numerical simulations might help to improve the output parameters as well, but are not accessible to date. Finally, cavity enhancement is an option that can be considered. To sum up, the latest experimental results [23] and scaling possibilities show that the intensities to generate high harmonics might be accessible in the near future with high repetition rates.
In conclusion, both experiments presented here are of great interest, for both research purposes and applications in the “real” world. Lensless imaging is presented as application of high-harmonic radiation. The generation of the spatially-coherent radiation in the EUV region is studied to estimate the required pulse parameters of the driving laser source. Today’s sources suffer from low repetition rate and long integration times. An approach that might help to solve this problem and provide faster HHG pump sources is presented and investigated in detail.

Bibliography

[1] A.L. Schawlow, C.H. Townes, *Infrared and Optical Masers*, Phys. Rev., **112**, 6, 1940-1949 (1958) 6, 24

[2] T.H. Maiman, *Stimulated Optical Radiation in Ruby*, Nature, **187**, 493-494 (1960) 6, 24, 36

[3] M.D. Perry, D.M. Pennington, B.C. Stuart, G. Tietbohl, J.A. Britten, C.G. Brown, S. Herman, B. Golick, M. Kartz, J.L. Miller, H.T. Powell, M. Vergino, V. Yanovsky, *"Petawatt laser pulses"*, Opt. Lett. **24**, 160-162 (1999) 6

[4] D.M. Pennington, J.A. Britten, J.L. Miller, M.D. Perry, C.G. Brown, G. Tietbohl, B.C. Stuart, S. Herman, V. Yanovsky, *"The Petawatt Laser System"*,UCRL-LR-105821-97-4
http://www.llnl.gov/nif/icf/icfpubs/qrtly_reports/jul-sep97/pennington.pdf 6

[5] H. Schwoerer, S. Pfotenhauer, O. Jäckel, K.-U. Amthor, B. Liesfeld, W. Ziegler, R. Sauerbrey, K. Ledingham, T. Esirkepov, *"Laser-plasma acceleration of quasi-monoenergetic protons from microstructured targets"*, Nature **439**, 445-448 (2006) 6

[6] K.W. D. Ledingham, R. Sauerbrey, *"Teilchenbeschleunigung und Unruh-Strahlung"*, Physik in unserer Zeit **1**, Nr. 37, 8-9 (2006) 6

[7] L.J. Perkins, B.G. Logan, M.D. Rosen, M.D. Perry, T. Diaz de la Rubia, N.M. Ghoniem, T. Ditmire, P.T. Springer, S.C. Wilks, *"The investigation of high intensity laser driven micro neutron sources for fusion materials research at high fluence"*, Nuclear Fusion **40**, 1-19 (2000), 6

[8] A. Zewail, *"Femtochemistry - Atomic scale dynamics of the chemical bond using ultrafast lasers"*, Nobel Lectures, Chemistry 1996-2000, Editor Ingmar Grenthe, World Scientific Publishing Co., Singapore (2003) 6

[9] P. Bastiaens, A. Squire, *"Fluorescence lifetime imaging microscopy: spatial resolution of biochemical processes in the cell"*, Trends in Cell Biology **9**, 48-51 (1999) 6

[10] P.A. Franken, A.E. Hill, C.W. Peters, G. Weinreich, *"Generation of optical harmonics"*, PRL **7**, 118-119 (1961) 6, 36, 38

[11] A. McPherson, G. Gibson, H. Jara, U. Johann, T. S. Luk, I. A. McIntyre, K. Boyer, and C. K. Rhodes, *"Studies of multiphoton production of vacuum-ultraviolet radiation in the rare gases"*, J. Opt. Soc. Am. B**4**, 595 (1987) 6, 9

[12] M Ferray, A L'Huillier, X F Li, L A Lompre, G Mainfray and C Manus, *"Multiple-harmonic conversion of 1064 nm radiation in rare gases"*, J. Phys. B**21**, L31 (1988) 6, 9

[13] E.A. Gibson, A. Paul, N. Wagner, R. Tobey, I.P. Christov, D.T. Attwood, E. Gullikson, A. Aquila, M.M. Murnane, H.C. Kapteyn, *"Coherent Soft X-ray Generation in the Water Window with Quasi-Phase Matching"*, Science **302**, 95-98 (2003) 6

[14] J. Seres, P. Wobrauschek, Ch. Streli, V. S. Yakovlev, E. Seres, F. Krausz, Ch. Spielmann, *"Generation of coherent keV x-rays with intense femtosecond laser pulses "*, New J. Phys. **8**, 1-11 (2006) 6

[15] M. Hentschel, R. Kienberger, Ch. Spielmann, G.A. Reider, N. Milosevic, T. Brabec, P. Corkum, U. Heinzmann, M. Drescher, F. Krausz, *Attosecond metrology*, Nature **414**, 509-513 (2001) 7

[16] A. Rundquist, C.G. Durfee III, Z. Chang, C. Herne, S. Backus, M.M. Murnane, H.C. Kapteyn, *"Phase-matched generation of coherent soft x-rays"*, Science **280**, 1412-1415 (1998) 7, 14

[17] J. Miao, P. Charalambous, J. Kirz, D. Sayre, *"Extending the methodology of X-ray crystallography to allow imaging of micrometer-sized non-crystalline specimen"*, Nature **400**, 342-344 (1999) 7, 16

[18] R.L. Sandberg, A. Paul, D.A. Raymondson, S. Hädrich, D.M. Gaudiosi, J. Holtsnider, R.I. Tobey, O. Cohen, M.M. Murnane, H.C. Kapteyn, *"Lensless Diffractive Imaging Using Tabletop Coherent High-Harmonic Soft-X-Ray Beams"*, PRL **99**,098103 (2007) 7, 19

[19] I. Matsushima, H. Yashiro, and T. Tomie, *"10 kHz 40 W Ti:sapphire regenerative ring amplifier"*, Opt. Lett. **31**, 2066-2068 (2006) 7

[20] A. Tünnermann, T. Schreiber, F. Röser, A. Liem, S. Höfer, H. Zellmer, S. Nolte, J. Limpert, *"The renaissance and bright future of fibre lasers"*, J. of Phys. B: At. Mol. Opt. Phys. **38**, S681-S693 (2005) 7, 24

[21] J. Limpert, F. Röser, T. Schreiber, A. Tünnermann, *"High-Power Ultrafast Fiber Laser Systems"*, IEEE J. of Select. Topics Quantum Electronic., **12**, 233-244 (2006) 7, 46, 57

[22] F. Röser, J. Rothhard, B. Ortaç, A. Liem, O. Schmidt, T. Schreiber, J. Limpert, A. Tünnermann, *"131 W 220 fs fiber laser system"*, Opt. Lett. **30**, 2754-2756 (2005) 7, 46

[23] F. Röser, T. Eidam, J. Rothhardt, O. Schmidt, D.N. Schimpf, J. Limpert, A. Tünnermann, *"Millijoule Pulse Energy High Repetition Rate Femtosecond Fiber CPA System "*, accepted for publication in Optics Letters 7, 46, 74

[24] R. Paschotta, J. Nilsson, A.C. Tropper, D.C. Hanna, *Ytterbium-Doped Fiber Amplifiers*, IEEE J. Quantum Electronic., **33**, 1049-1056 (1997) 7, 27, 28, 46

[25] A. Baltuška, T. Kobayashi, *"Adaptive shaping of two-cycle visible pulses using a flexible mirror"*, Appl. Phys. B **75**, 427-443 (2002) 7, 41

[26] A. Killi, A. Steinmann, G. Palmer, U. Morgner, H. Bartelt, and J. Kobelke, *"Megahertz optical parametric amplifier pumped by a femtosecond oscillator"*, Opt. Lett. **31**, 125-127 (2006) 7, 47

[27] C. Aguergaray, T. V. Andersen, D. N. Schimpf, O. Schmidt, J. Rothhardt, T. Schreiber, J. Limpert, E. Cormier, and A. Tünnermann, *"Parametric amplification and compression to ultrashort pulse duration of resonant linear waves"*, Opt. Express **15**, 5699-5710 (2007) 7, 47

[28] T.V. Andersen, O. Schmidt, C. Bruchmann, J. Limpert, C. Aguergaray, E. Cormier, A. Tünnermann, *"High repetition rate tunable femtosecond pulses and broadband*

amplification from fiber laser pumped parametric amplifier", Opt. Express **14**, 4765-4773 (2006) 7

[29] E. Constant, E. Mével, *"Attosecond Pulses"*, in: C. Rullière, *"Femtosecond Laser Pulses - Principles and Experiments"*, Second Edition, Springer (2005) 9

[30] K.C. Kulander, K. J. Schafer and J.L. Krause, *"in Proceedings of the Workshop, Super Intense Laser Atom Physics (SILAP) III"* 10

[31] P. B. Corkum, *"Plasma Perspective on Strong-Field Multiphoton Ionization"*, Phys. Rev. Lett. **71**, 1995 (1993) 10

[32] M.V. Ammosov, M.B. Delone, V.P. Krainov, Sov. Phys. JETP **64**, 1191 (1986) 11

[33] M. Lewenstein, Ph. Balcou, M. Yu. Ivanov, A. L'Huilier and P.B. Corkum, *"Theory of high-harmonic generation by low-frequency laser fields"*, Phys. Rev.A **49**(3), 2117 (1994) 14

[34] Ariel Paul, *"Coherent EUV Light from High-Order Harmonic Generation: Enhancement and Applications to Lensless Diffractive Imaging"*, Phd Thesis, Kapteyn Murnane Research Group, JILA, Boulder (Colorado), 2007 15

[35] C. G. Durfee III, A. R. Rundquist, S. Backus, C. Herne, M. M. Murnane, H. C. Kapteyn, *"Phase matching of high-order harmonics in hollow waveguides"*, Phys. Rev. Lett. **83**, 2187–2190 (1999) 15

[36] I. Christov, H.C. Kapteyn, M.M. Murnane, *"Quasi-phase matching of high harmonics and attosecond pulses in modulated waveguides"*, Opt. Exp. **7**, 362–367 (2000) 15

[37] I. P. Christov, *"Control of high harmonic and attosecond pulse generation in aperiodic modulated waveguides"*, J. Opt. Soc. Am. B. **18**, 1877–1881 (2001) 15

[38] H.C. Kapteyn, M.M. Murnane, I.P. Christov, *"Extreme Nonlinear Optics: Coherent X Rays from Lasers"*, Physics Today, March 2005, 39-45 16

[39] A. Paul, R. Bartels, R. Tobey, H. Green, S. Weiman, I. Christov, M. Murnane, H. Kapteyn, S. Backus, *"Quasi-phase-matched generation of coherent extreme-ultraviolet light"*, Nature **421**, 51-54 (2003) 16

[40] J. Miao, D. Sayre, H.N. Chapman, *"Phase retrieval from the magnitude of the Fourier transform of nonperiodic objects"*, J. Opt. Soc. Am. A **15**, 1662-1669 (1998) 17

[41] J. Miao, D. Sayre, *"On possible extensions of X-ray crystallography through diffraction-pattern oversampling"*, Acta Cryst. A **56**, 596-605 (2000) 17

[42] J. Miao, T. Ishikawa, E.H. Anderson, K.O. Hodgson, *"Phase retrieval of diffraction patterns from noncrystalline samples using the oversampling method"*, Phys. Rev. B **67**, 174104 (2003) 19

[43] S. Backus, J. Peatross, C. P. Huang, M. M. Murnane, H. C. Kapteyn, *"Ti:sapphire amplifier producing millijoule-level, 21-fs pulses at 1 kHz"*, Opt. Lett. **20**, 2000-2002 (1995) 19

[44] www.quantifoil.com 21

[45] C.J. Koester, E. Snitzer, *"Amplification in a Fiber Laser"*, Appl. Opt. **3**, 1182-1186 (1964) 24

[46] Govind P. Agrawal, *"Nonlinear Fiber Optics"*, Academic Press, San Diego (2001) 25, 32, 33, 35

[47] H. Zellmer, A. Tünnermann, H. Welling , *"Double-Clad Fiber Laser with 30 W Output Power"*, OSA TOPS Vol.**16**, Optical Amplifiers and Their Applications, Optical Society of America (1997) 26

[48] J. Riishede, N.A. Mortensen, J. Lægsgaard, *"A poor man's approach to modelling micro-structured optical fibers"*, J. Opt. A: Pure Appl. Opt. **5**, 534-538 (2003) 25

[49] J.C. Knight, *"Photonic crystal fibres"*, Nature **424**, p. 847-851 (2003) 27

[50] C.D. Brooks, F. Di Teodoro, *"Multimegawatt peak-power, single-transverse-mode operation of a 100 μm core diameter, Yb-doped rodlike photonic crystal fiber amplifier"*, Appl. Phys. Lett. **89**, 111119 (2006) 27

[51] http://www.crystal-fibre.com/support/dictionary.shtm 27

[52] H.W. Etzel, H.W. Gandy, R.J. Ginther, *"Stimulated emission of infrared radiation from ytterbium-activated silicate glass"*, Appl. Opt., **1**, 534 (1962) 27

[53] H.M. Pask, R.J. Carman, D.C. Hanna, A.C. Tropper, C.J. Mackechnie, P.R. Barber, J.M. Dawes, *"Ytterbium-Doped Silica Fiber Lasers: Versatile Sources for the 1-1.2μm region"*, IEEE J. of Select. Topics Quantum Electronic., **1**, 2-13 (1995) 27, 28

[54] www.rp-photonics.com 28

[55] B.E.A. Saleh, M.C. Teich, *"Fundamentals of Photonics"*, 2^nd edition, Wiley (2007) 29, 33

[56] I. Walmsley, L. Waxer, C. Dorrer, *"The role of dispersion in ultrafast optics"*, Rev. Sci. Instrum., Vol. **72**, 1-29 (2001) 30, 31

[57] D. Strickland, G. Mourou, *"Compression of amplified chirped optical pulses"*, Opt. Commun. **55**, 447-449 (1985) 31

[58] R. Szipöcs, K. Ferencz, C. Spielmann, F. Krausz, *"Chirped multilayer coatings for broadband dispersion control in femtosecond lasers"*, Opt. Letters **19**, 201-203 (1994) 31

[59] T. Schreiber, *"Taylored optical properties of microstructured fibers"*, Phd Thesis, Jena, 2006 29, 33

[60] J.M. Dudley, *"Supercontinuum generation in photonic crystal fiber"*, Rev. Mod. Phys. **78**, 1135-1184 (2006) 34

[61] J.A. Armstrong, N. Bloembergen, J. Ducuing, P.S. Pershan, *"Interactions between Light Waves in a Nonlinear Dielectric"*, Phys. Rev. **127**, 1918-1939 (1962) 36, 39

[62] P.N. Butcher, D. Cotter, *"The Elements of Nonlinear Optics"*, Cambridge Studies in Modern Optics, Cambridge University Press, 1991 36, 37

[63] Y.R. Shen, *"The Principles of Nonlinear Optics"*, John Wiley & Sons, 1984 37

[64] R.L. Sutherland, *"Handbook of Nonlinear Optics"*, Marcel Dekker, 1996 37, 38, 39, 40, 67

[65] Personal notes, lecture: Nonlinear Optics, Prof. Lederer, summer term 2005, University Jena 38

[66] J.M. Manley, H.E. Rowe, *"Some General Properties of Nonlinear Elements - Part I. General Energy Relations"*, Proc. of IRE **44**, 904-913 (1956) 38

[67] R.W. Boyd, *"Nonlinear Optics"*, Second Edition, Academic Press, 2003 39

[68] G. Cerrullo, S. De Silvestri, *"Ultrafast optical parametric amplifier"*, Rev. Sci. Instrum. **74**, 1-18 (2003) 41, 45, 64

[69] M.M. Feier, E.L. Ginzton, *"Nonlinear frequency conversion in microstructured materials"*, Lasers and Electro-Optics, 1995. Technical Digest. CLEO/Pacific Rim'95., Pacific Rim Conference on 10-14 July 1995 Page(s):109 41

[70] A. Dubietis, G. Jonusasuskas, A. Piskarkas, *"Powerful femtosecond pulse generation by chirped and stretched pulse parametric amplification in BBO crystal"*, Opt. Commun. **88**, 437 (1992) 44

[71] S. Backus, C.G. Durfee III, M.M. Murnane, H.C. Kapteyn, *"High power ultrafast lasers"*, Rev. Sci. Instrum. **69**, 1207-1223 (1998) 46

[72] J. Dudley and S. Coen, *"Fundamental limits to few-cycle pulse generation from compression of supercontinuum spectra generated in photonic crystal fiber"*, Opt. Express **12**, 2423-2428 (2004) 47

[73] T. M. Fortier, D. J. Jones, and S. T. Cundiff, *"Phase stabilization of an octave-spanning Ti:sapphire laser"*, Opt. Lett. **28**, 2198-2200 (2003) 47

[74] P. F. Moulton, Solid State Research Rep. DTIC ADA124305/ 4 (MIT Lincoln Laboratory, Lexington, Mass.), pp. 15-21, 1982 48

[75] U. Keller, G.W. ´tHooft, W.H. Knox, J.E. Cunningham, *"Femtosecond pulses from a continuously self-starting passively mode-locked Ti:sapphire laser"*, Opt. Letters **16**, 1022-1024 (1991) 48

[76] A. Pistolek, *"Entwicklung eines OPCPA-Systems zur Verstärkung ultrakurzer Pulse bis in den Terawattbereich"*, Dissertation, Heinrich Heine Universität Düsseldorf, Institut für Laser- und Plasmaphysik, Dezember 2006 48

[77] H. Frowein, *"Titan-Saphir Laser - Grundlagen und Anwenungen des wichtigsten Kurzpulslasersystems"*, Optik & Photonik, März 2007 48

[78] M. Ramaswamy, M. Ulmann, J. Paye, J.G. Fujimoto, *"Cavity-dumped femtosecond Kerr-Lens mode-locked $Ti:Al_2O_3$ laser"*, Opt. Letters **18**, 1822-1824 (1993) 48

[79] http://www.kmlabs.com/laser_cascade.htm 49

[80] www.fiberdesk.com 50

[81] M.D. Perry, T. Ditmire, B.C. Stuart, *"Self-phase modulation in chirped-pulse amplification"*, Opt. Lett. **19**, 2149-2151 (1994) 57

[82] Gregor Stobrawa, *"Aufbau und Anwendungen eines hochauflösenden Impulsformers zur Kontrolle ultrakurzer Laserimpulse"*, Dissertation, IOQ Jena, 2003 59

[83] K.H. Liao, A.G. Mordovanakis, G. Chang, M. Rever, G. Mourou, J. Nees, A. Galvanauskas, *'Generation of hard X-rays using an ultafast fiber laser system"*, Opt. Expr. **15**, 13942-13948, (2007) 59

[84] http://www.crystal-fibre.com/datasheets/DC-200-40-PZ-Yb-01.pdf 60

[85] http://www.ekspla.com/repository/catalogue/pdfai/NLOC/LBO.pdf e 62

[86] http://www.sandia.gov/imrl/X1118/xxtal.htm 63

[87] L. Hongjun, Z. Wei, C. Guofu, W. Yishan, C. Zhao and R. Chi, *"Investigation of spectral bandwidth of optical parametric amplification"*, Appl. Phys. B **79**, 569-576 (2004) 64

[88] S. Witte, R.T. Zinkstok, W. Hogervorst, K.S.E. Eikema, *"Numerical simulations for performance optimization of a few-cycle terawatt NOPCPA system"*, Appl. Phys. B **87**, 677-684 (2007) 66, 67

[89] W. F. Schlotter, R. Rick, K. Chen, A. Scherz, J. Stöhr, and J. Lüning, S. Eisebitt, Ch. Günther, W. Eberhardt, O. Hellwig, I. McNulty, *"Multiple reference Fourier transform holography with soft x rays"*, Appl. Phys. Lett. **89**, 163112 (2006) 73

Erklärung:

Ich erkläre, dass ich die vorliegende Arbeit selbstständig verfasst und keine anderen als die angegebenen Quellen und Hilfsmittel benutzt habe.

Jena, der..... Steffen Hädrich.....

Seitens des Verfassers bestehen keine Einwände, die vorliegende Diplomarbeit für die Nutzung in der Thüringer Universitäts- und Landesbibliothek zur Verfügung zu stellen.

Jena, der..... Steffen Hädrich.....